

Impact of mineral dust on the global nitrate aerosol direct and indirect radiative effect

Alexandros Milousis¹, Klaus Klingmüller², Alexandra P. Tsimpidi¹, Jasper F. Kok³, Maria Kanakidou^{4,5,6}, Athanasios Nenes^{5,7}, and Vlassis A. Karydis¹

¹Institute of Climate and Energy Systems: Troposphere (ICE-3), Forschungszentrum Jülich GmbH, Jülich, Germany

²Max Planck Institute for Chemistry, Mainz, Germany

³Department of Atmospheric and Oceanic Sciences, University of California Los Angeles, Los Angeles, CA, USA.

⁴Environmental Chemical Processes Laboratory, Department of Chemistry, University of Crete, Heraklion, Greece

⁵Center for the Study of Air Quality and Climate Change, Foundation for Research & Technology Hellas, Patras, Greece

⁶Institute of Environmental Physics, University of Bremen, Bremen, Germany

⁷Laboratory of Atmospheric Processes and Their Impacts, Ecole Polytechnique Fédérale de Lausanne, Switzerland

Correspondence to: Vlassis A. Karydis (v.karydis@fz-juelich.de)

Abstract

Nitrate (NO_3^-) aerosol is projected to increase dramatically in the coming decades and may become the dominant inorganic particle species. This is due to the continued strong decrease in SO_2 emissions, which is not accompanied by a corresponding decrease in NO_x and especially NH_3 emissions. Thus, the radiative effect (RE) of NO_3^- aerosol may become more important than that of SO_4^{2-} aerosol in the future. The physicochemical interactions of mineral dust particles with gas and aerosol tracers play an important role in influencing the overall RE of dust and non-dust aerosols but can be a major source of uncertainty due to their lack of representation in many global climate models. Therefore, this study investigates how and to what extent dust affects the current global NO_3^- aerosol radiative effect through both radiation (RE_{ari}) and cloud interactions (RE_{aci}) at the top of the atmosphere (TOA). For this purpose, multi-year simulations nudged towards the observed atmospheric circulation were performed with the global atmospheric chemistry and climate model EMAC, while the thermodynamics of the interactions between inorganic aerosols and mineral dust were simulated with the thermodynamic equilibrium model ISORROPIA-lite. The emission flux of the mineral cations Na^+ , Ca^{2+} , K^+ and Mg^{2+} is calculated as a fraction of the total aeolian dust emission based on the unique chemical composition of the major deserts worldwide. Our results reveal positive and negative shortwave and longwave radiative effects in different regions of the world via aerosol-radiation interactions and cloud adjustments. Overall, the NO_3^- aerosol direct effect contributes a global cooling of -0.11 W/m^2 , driven by fine-mode particle cooling at short wavelengths. Regarding the indirect effect, it is noteworthy that NO_3^- aerosol exerts a global mean warming of $+0.17 \text{ W/m}^2$. While the presence of NO_3^- aerosol enhances the ability of mineral dust particles to act as cloud condensation nuclei (CCN), it simultaneously inhibits the formation of cloud droplets from the smaller anthropogenic particles. This is due to the coagulation of fine anthropogenic CCN particles with the larger nitrate-coated mineral dust particles, which leads to a reduction in total aerosol number concentration. This mechanism results in an overall reduced cloud albedo effect and is thus attributed as warming.

Keywords: direct radiative effect, indirect radiative effect, nitrate aerosols, mineral dust

41 1. Introduction

42 Atmospheric aerosols are among the most complex components of the Earth's climate system.
43 This is due not only to the diversity of their origins, with many natural and anthropogenic emission
44 sources, but also to their extremely varied chemical composition and properties. The many
45 mechanisms by which they interact with each other and with physical entities such as radiation,
46 clouds, land, and oceans add to their complexity and play a critical role in the energy balance of
47 the planet (Arias et al., 2021). The most direct way in which aerosols affect the Earth's energy
48 balance is through their interactions with solar shortwave (SW) and terrestrial longwave (LW)
49 radiation (IPCC, 2013). Overall, the radiative effect due to aerosol-radiation interactions (RE_{ari}) is
50 mainly dominated by the scattering of SW radiation back to space (negative radiative effect,
51 generating a cooling of the climate system) and the absorption of LW radiation (positive radiative
52 effect, generating a warming of the climate system) (Gao et al., 2018; Tsigaridis and Kanakidou,
53 2018). Aerosols belonging to the black and/or brown carbon family, together with mineral dust
54 particles, contribute to absorption (Kanakidou et al., 2005; Zhang et al., 2017; Wong et al., 2019),
55 while the main inorganic aerosol components, such as sulfate and nitrate, as well as a significant
56 amount of organic carbon contribute mainly to scattering (Kirchstetter et al., 2004; (Bond and
57 Bergstrom, 2006; Klingmüller et al., 2019; Zhang, 2020). However, mineral dust can also
58 influence the behavior of the RE_{ari} of anthropogenic pollution. Dust particles alter the
59 anthropogenic radiative effect of aerosol-radiation interactions by reducing the loading of
60 anthropogenic aerosols (either by coagulating with them or by adsorption of their precursor
61 inorganic trace gases), leading to less scattering of solar radiation and thus a warming effect (Kok
62 et al., 2023).

63 Atmospheric aerosols can also indirectly affect the Earth's energy balance by forming clouds,
64 controlling cloud optical thickness and scattering properties, and altering their precipitation and
65 lifetime (IPCC, 2013). Atmospheric aerosols act as cloud condensation nuclei (CCN), providing a
66 suitable surface for water vapor to condense, leading to the formation of liquid droplets that
67 develop into a corresponding liquid cloud (Lance et al., 2004). Such clouds are referred to as warm
68 clouds and are typically found in the lower troposphere (Khain and Pinsky, 2018). However, there
69 is constant competition between small and large particles for the available amount of water vapor
70 (Barahona et al., 2010; Morales and Nenes, 2014). Under the same humidity conditions, the
71 presence of small particles will lead to the formation of small droplets with high number
72 concentrations, while the presence of larger particles will lead to the formation of large droplets
73 but with lower number concentrations. Depending on the size characteristics of its particle
74 population, a warm cloud will exhibit different optical properties, with a population dominated by
75 smaller particles generally being more reactive in the SW spectrum. The change in cloud
76 reflectivity due to the presence of aerosols is referred to as the first radiative effect due to aerosol-
77 cloud interactions (RE_{aci}) and was first described by Twomey (1977). The small size of
78 anthropogenic aerosols results in an overall smaller cloud droplet size, which reduces precipitation
79 efficiency and thus increases cloud lifetime. This contributes to cloud reflectivity and is referred
80 to as the second radiative effect of aerosol cloud-interactions, first described by Albrecht (1989).
81 These two indirect effects are considered equally important for the total indirect radiative effect of
82 aerosols (Lohmann and Feichter, 2005). Atmospheric aerosols exert a net cooling effect that can
83 partially mask the warming effect of greenhouse gases, therefore, the recent decline in

84 anthropogenic aerosol concentrations may accelerate global warming (Urdiales-Flores et al.,
85 2023). Overall, the radiative effect due to aerosol-cloud interactions is considered the main source
86 of existing uncertainty in the effective (total) radiative effect of aerosols in the atmosphere (Myhre
87 et al., 2014; Seinfeld et al., 2016).

88 Mineral dust influences the anthropogenic radiative effect through aerosol-cloud interactions in
89 several ways that can result in either a net warming or net cooling effect. Dust particles can increase
90 the of cloud droplet number concentrations (CDNC) in remote areas since through chemical aging
91 by pollutants (Nenes et al., 2014; Karydis et al., 2017), dust particles become more hygroscopic
92 and require lower supersaturation thresholds for activation (Karydis et al., 2011). This is caused
93 by the transfer of anthropogenic pollutants towards remote desert regions which enhances the
94 solubility of dust particles. In such regions, this mostly results in increased cloud albedo and a net
95 cooling effect. However, dust particles also tend to reduce the availability of smaller anthropogenic
96 CCN. This is due to intrusions of aged dust particles into polluted environments which reduce the
97 numbers of smaller aerosols through increased coagulation with them. This results in lower cloud
98 reflectivity (albedo) and thus a net warming effect (Klingmüller et al., 2020). Furthermore, when
99 dust is above or below low-level clouds, the resulting effect of local heating is an increase in total
100 cloud cover due to enhanced temperature inversion or enhanced upward vertical motion,
101 respectively (Kok et al., 2023). On the other hand, when dust is present inside low-level clouds,
102 local heating enhances in-cloud evaporation, resulting in an overall decrease in cloud cover. Kok
103 et al. (2023) showed that the amount of desert dust in the atmosphere has increased since the mid-
104 19th century, causing an overall cooling effect on the Earth that masks up to 8% of the warming
105 caused by greenhouse gases. If the increase in dust were halted, the previously hidden additional
106 warming potential of greenhouse gases could lead to slightly faster climate warming.

107 NO_3^- is expected to dominate the global aerosol composition in the coming decades due to the
108 predicted limited availability of SO_4^{2-} following the abrupt decline in SO_2 emissions, which will
109 not necessarily be accompanied by proportional reductions in NO_x and NH_3 emissions (Bellouin
110 et al., 2011; Hauglustaine et al., 2014). Excess NO_3^- is expected to exert a cooling RE_{ari} by
111 scattering SW radiation (Bauer et al., 2007a; Xu and Penner, 2012; Myhre et al., 2013; IPCC,
112 2013; Li et al., 2015), but the RE_{aci} is much more complex and complicated and can lead to both
113 cooling and warming. Mineral dust thus becomes a key factor, as it is one of the main promoters
114 of NO_3^- aerosol formation, providing a very suitable surface for gaseous HNO_3 condensation to
115 the aerosol phase (Karydis et al., 2011; Trump et al., 2015). In addition to HNO_3 adsorption,
116 heterogeneous reactions on the surface of dust particles are known to promote nitrate formation
117 (Krueger et al., 2004; Hodzic et al., 2006). The most important pathway through which this occurs
118 is N_2O_5 hydrolysis with a yield for aerosol nitrate of ~ 2 (Seisel et al., 2005; Tang et al., 2012). At
119 the same time, other reactions, such as NO_2 oxidation, contribute to much slower nitrate production
120 and are of major importance mainly during short periods of dust pollution events (Li et al., 2024).
121 These processes affect not only the optical properties of dust aerosols, which will influence their
122 overall RE_{ari} , but also how they can alter cloud formation and microphysics. NO_3^- aerosols increase
123 the hygroscopicity of mineral dust (Kelly et al., 2007) by providing layers of soluble material on
124 their surface, thus increasing their ability to act as CCN (Karydis et al., 2017). In doing so, they
125 also increase the size of dust particles through hygroscopic growth and therefore their coagulation
126 efficiency. Thus, nitrate-dust interactions are a complex mechanism that ultimately affects

127 climatology in a variety of ways. The role of mineral dust in modifying the influence of NO_3^-
128 aerosols in the global RE_{aci} is not yet well understood. This study aims to focus on the extent of
129 the RE_{ari} and RE_{aci} of NO_3^- aerosols and on how interactions with mineral dust regulate both on a
130 global scale.

131 This study is organized as follows: in Section 2, details of the modeling setup for conducting
132 the global simulations as well as the treatment of dust-nitrate interactions in the model are
133 discussed and the methodology for calculating the global RE_{ari} and RE_{aci} of NO_3^- aerosols is
134 explained. Section 3 presents the main results for the global RE_{ari} for coarse and fine NO_3^- aerosols
135 for the base case simulation and the sensitivity cases listed in Table 1. Section 4 presents the results
136 for the global RE_{aci} of total NO_3^- aerosols, while section 5 includes the feedback mechanism of
137 dust-nitrate interactions with cloud microphysics. Finally, the main conclusions and a general
138 discussion on the scope of the study are presented in section 6.

139 **2. Methodology**

140 **2.1 Model Setup**

141 The simulations were performed with the global atmospheric chemistry and climate model
142 EMAC (ECHAM/MESSy) (Jockel et al., 2006), which includes several submodels describing
143 atmospheric processes and their interactions with oceans, land, and human influences. These
144 submodels are linked through the Modular Earth Submodel System (MESSy) (Jockel et al., 2005)
145 to a base model, the 5th Generation European Center Hamburg General Circulation Model
146 (ECHAM) (Roeckner et al., 2006). The submodel system used in this work includes the MECCA
147 submodel, which performs the gas phase chemistry calculations (Sander et al., 2019). The SCAV
148 submodel is responsible for the in-cloud liquid-phase chemistry and wet deposition processes (Tost
149 et al., 2006; Tost et al., 2007b), while DRYDEP and SEDI are used to compute the dry deposition
150 of gases and aerosols and gravitational settling, respectively (Kerkweg et al., 2006). All aerosol
151 microphysical processes are calculated by the GMXe submodel (Pringle et al., 2010a; Pringle et
152 al., 2010b), where aerosols are divided into 4 lognormal size modes (nucleation, Aitken,
153 accumulation and coarse). Each mode is defined in terms of aerosol number concentration, number
154 mean dry radius, and geometric standard deviation (sigma). The mean dry radius for each mode is
155 allowed to vary within fixed bounds (0.5 nm – 6 nm for nucleation, 6 nm - 60 nm for Aitken, 60
156 nm - 700 nm for accumulation, and above 700 for coarse) and the sigma is fixed and equal to 1.59
157 for the first three size modes and 2 for the coarse mode. The coagulation of aerosols is also handled
158 by GMXe, following Vignati et al. (2004) and the coagulation coefficients for Brownian motion
159 are calculated according to Fuchs and Davies (1964). The partitioning between the gas and aerosol
160 phases is calculated using the ISORROPIA-lite thermodynamic module (Kakavas et al., 2022) as
161 implemented in EMAC by Milousis et al. (2024). The optical properties of the aerosols and the
162 radiative transfer calculations are simulated by the submodels AEROPT (Dietmuller et al., 2016)
163 and RAD (Dietmuller et al., 2016), respectively. AEROPT can be called several times within a
164 model time step with different settings for the aerosol properties. More details are given in section
165 2.3.1. All cloud properties and microphysical processes are simulated by the CLOUD submodel
166 (Roeckner et al., 2006) using the two-moment microphysical scheme of Lohmann and Ferrachat
167 (2010) for liquid and ice clouds. The activation processes of liquid cloud droplets and ice crystals
168 follow the physical treatment of Morales and Nenes (2014) and Barahona and Nenes (2009),

169 respectively, as described by Karydis et al. (2017) and Bacer et al. (2018). More details are given
170 in Section 2.3.2.

171 The meteorology for each of the simulations was nudged by ERA5 reanalysis data (C3S, 2017),
172 thus this study estimates the radiative effect of nitrate aerosols with respect to RE_{ari} and RE_{aci}
173 separately, rather than the effective (total) radiative effect, as this would require multiple free-run
174 simulations with prescribed sea surface temperatures for each case separately. The spectral
175 resolution used for each simulation was T63L31, which corresponds to a grid resolution of
176 $1.875^\circ \times 1.875^\circ$ and 31 vertical layers up to 25 km in height. The period covered by the
177 simulations is from 2007 to 2018, with the first year representing the model spin-up period.

178 Anthropogenic aerosol and trace gas emissions were taken from the CMIP6 database (O'Neill
179 et al., 2016) according to the SSP370 scenario. Natural NH_3 emissions (from land and ocean) were
180 based on the GEIA database (Bouwman et al., 1997), and natural volcanic SO_2 emissions were
181 taken from the AEROCOM database (Dentener et al., 2006). Biogenic NO emissions from soils
182 were calculated online according to the algorithm of Yienger and Levy (1995), while lightning-
183 produced NO_x was also calculated online by the LNOx submodel (Tost et al., 2007a) using the
184 parameterization of Grewe et al. (2001). DMS emissions from the oceans are calculated online by
185 the AIRSEA submodel (Pozzer et al., 2006). Sea salt emissions are based on the AEROCOM
186 database (Dentener et al., 2006) following the chemical composition reported by Seinfeld and
187 Pandis (2016), i.e. 30.6% Na^+ , 3.7% Mg^{2+} , 1.2% Ca^{2+} , 1.1% K^+ , and 55% Cl^- . Dust emissions are
188 calculated online using the parameterization of Astitha et al. (2012). In this scheme, while the
189 surface friction velocity is the most important parameter for the amount of the emitted dust flux,
190 the meteorological information for each grid cell is also taken into account. Dust particles are
191 emitted in the accumulation and coarse size modes of the insoluble fraction but can be transferred
192 to the soluble fraction after either coagulation with other soluble species and/or by condensation
193 of soluble material on their surface. Both processes are treated and calculated by GMXe and
194 ISORROPIA-lite. The emissions of mineral ions (Ca^{2+} , Mg^{2+} , K^+ , and Na^+) are estimated as a
195 fraction of the total dust emission flux based on the soil chemical composition of each grid cell.
196 This is done using desert soil composition maps from Klingmüller et al. (2018) which are based
197 on the mineral ion fractions from Karydis et al. (2016). These mineral ions are treated as individual
198 species that are part of the aerosol in each size mode and are assumed to be well mixed with the
199 rest of the aerosol species considered (i.e., dust, black carbon, organics, inorganic ions). The
200 aerosol composition within each of the seven modes considered is uniform in size (internally
201 mixed), but may vary between modes (externally mixed).

202 To assess the impact of changes in mineral dust chemistry and emissions on the global NO_3^-
203 aerosol RE_{ari} and RE_{aci} , four additional sensitivity simulations were performed (Table 1). In the
204 first sensitivity simulation, mineral dust is described only by a bulk, chemically inert species. In
205 this case, there is no uptake of HNO_3 by the dust particles due to acid-base interactions with the
206 non-volatile cations (NVCs), and so it remains in the gas phase. In the second sensitivity case, the
207 chemical composition of the mineral dust was assumed to be spatially uniform, with a percentage
208 distribution for bulk dust, Na^+ , K^+ , Ca^{2+} and Mg^{2+} particles assumed to be 94%, 1.2%, 1.5%, 2.4%
209 and 0.9% respectively according to Sposito (1989). Finally, two additional simulations were
210 performed to assess the impact of the global mineral dust budget on the results, where the dust
211 emission fluxes were first halved and then increased by 50% to account for the historical increase

212 in global dust mass load since pre-industrial times, as reconstructed by Kok et al. (2023). The
213 particle size distribution of the emitted dust mass remained unchanged in all sensitivity
214 simulations.

215 Overall, the EMAC model is well established in the literature for its ability to accurately predict
216 organic and inorganic aerosol concentrations and compositions, aerosol optical depth, acid
217 deposition, gas-phase mixing ratios, cloud properties, and meteorological parameters (de Meij et
218 al., 2012; Pozzer et al., 2012, 2022; Tsimpidi et al., 2016, 2017; Karydis et al., 2016, 2017; Bacer
219 et al., 2018; Milousis et al., 2024), factually replicate dust emissions (Astitha et al., 2012;
220 Abdelkader et al., 2015; Klingmüller et al., 2018), and provide realistic estimates for CCN and
221 CDNC (Chang et al., 2017; Karydis et al., 2017; Fanourgakis et al., 2019). Here, a comparison of
222 the performance of the model in estimating the surface mass concentrations of $\text{PM}_{2.5}$ NO_3^- and
223 total PM_{10} aerosols is provided in the supplemental material (Figures S2, S3 and Tables S1, S2).
224 In addition, the ability of the model to estimate CDNCs is evaluated (Figure S4 and Table S3).
225 The comparison is made with observations of $\text{PM}_{2.5}$ nitrate aerosols from regional networks in the
226 polluted northern hemisphere covering the regions of East Asia (EANET, The Acid Deposition
227 Monitoring Network in East Asia), Europe (EMEP, European Monitoring and Evaluation
228 Programme) and the USA for urban (EPA-CASTNET, U.S. Environmental Protection Agency
229 Clean Air Status and Trends Network) and rural (IMPROVE, Interagency Monitoring of Protected
230 Visual Environments) locations. The comparison with observations of surface mass PM_{10} aerosols
231 also covers the above mentioned monitoring networks, with the exception of the EPA. Finally, the
232 CDNCs estimated by the base case simulation are compared with the CDNCs observed in different
233 regions of the planet (continental, polluted and clean marine) over different time periods, but also
234 altitudes, as found in Karydis et al., (2017) and all relevant references therein.

235

236 **Table 1:** Differences between the base case and all sensitivity simulations performed.

Simulation Name	Conditions Applied
Base Case	Mineral dust ion composition according to Karydis et al. (2016) ¹
<u>Sensitivity 1:</u> Chemically Inert Dust	Mineral dust emitted exclusively as a chemically inert bulk particle
<u>Sensitivity 2:</u> Homogeneous Ion Composition	Global homogeneous ionic composition of mineral dust particles according to Sposito (1989) ²
<u>Sensitivity 3:</u> Half Dust Scenario	50% reduced dust emission flux
<u>Sensitivity 4:</u> Increased Dust Scenario	50% increased dust emission flux

237

238

239 **2.2 Treatment of Dust-Nitrate Interactions**

240 The interactions between mineral dust and nitrate aerosols play a crucial role in altering the size
 241 distribution and optical properties of both species and can also strongly influence cloud
 242 microphysical processes (Fig. 1). Therefore, these interactions affect both the RE_{ari} and the RE_{aci}
 243 of both nitrate and dust aerosols. First, the adsorption of HNO_3 onto the surface of dust particles
 244 is a process that strongly promotes the formation of nitrate aerosols on dust (Karydis et al., 2016).
 245 We treat this condensation process using the GMXe submodel. Specifically, the amount of gas
 246 phase species that kinetically condenses within a model time step (equal to 10 minutes in this
 247 study) is calculated according to the diffusion-limited condensation theory of Vignati et al. (2004).
 248 The diffusive flux of gas on a single particle surface for each size mode i is described by the

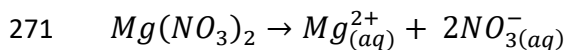
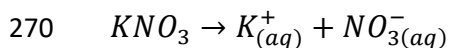
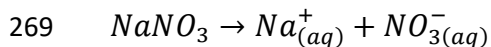
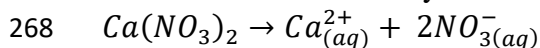
¹ The ionic composition of the dust particles with respect to the mineral ions Ca^{2+} , Mg^{2+} , K^+ , and Na^+ depends on the chemical composition of the soil in each grid cell, which is estimated from the desert soil composition maps of Klingmüller et al. (2018) based on the fraction of mineral ions present found in Karydis et al. (2016).

² The ionic composition of the dust particles is homogeneous and held constant in all grid cells where dust is present. The dust particles are a mixture of bulk species and the mineral ions Na^+ , K^+ , Ca^{2+} and Mg^{2+} with mass fraction of 94%, 1.2%, 1.5%, 2.4% and 0.9% respectively.

249 condensation coefficient C_i according to Fuchs and Davies (1964) and is estimated from the
 250 following function as found in Vignati et al. (2004).

$$251 \quad C_i = \frac{4\pi D r_{gi}}{\frac{4D}{svr_{gi}} + \frac{r_{gi}}{r_{gi} + \Delta}}$$

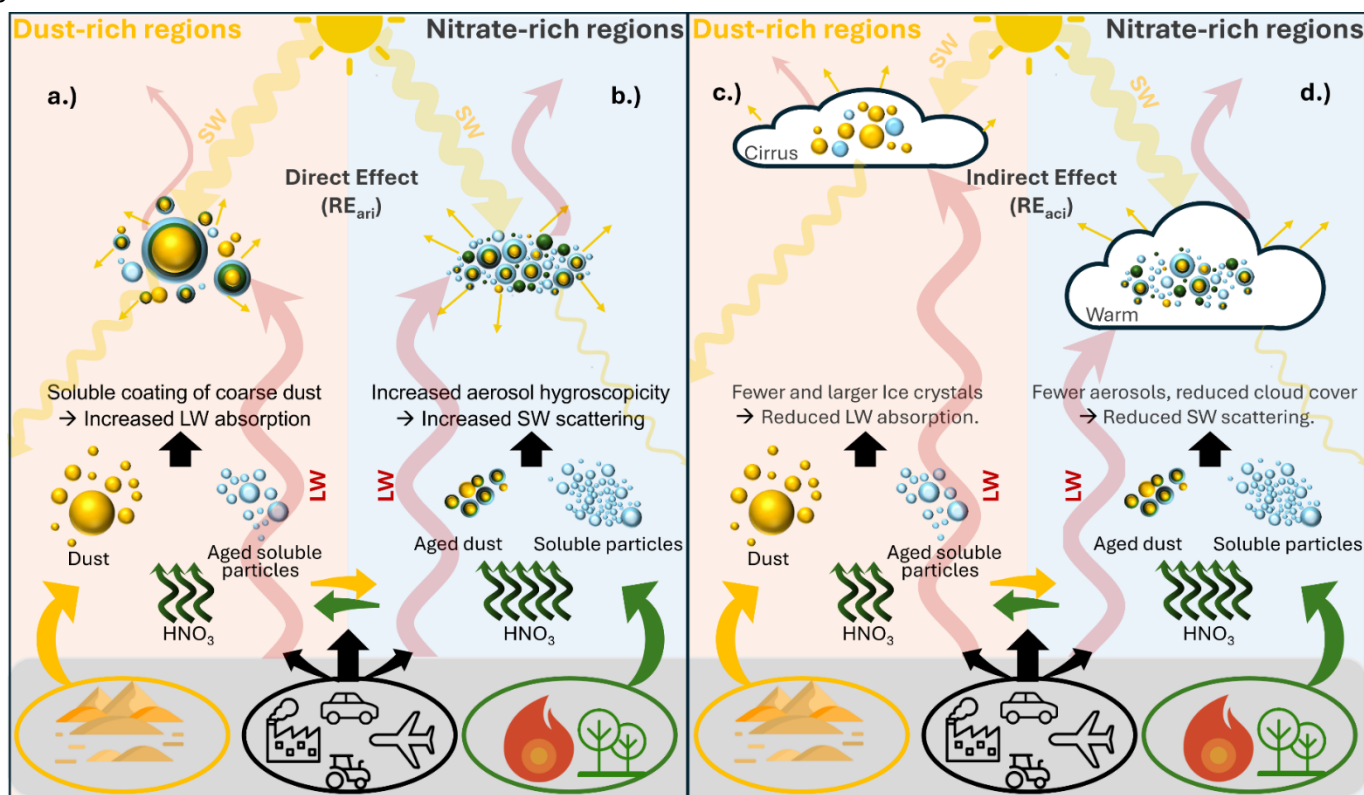
252 Where r_{gi} is the geometric mean radius of the size mode i , D is the diffusion coefficient, s is an
 253 accommodation coefficient for each gas species treated and has the assigned values of 1 for H_2SO_4
 254 (Vignati et al. 2004), 0.1 for HNO_3 , 0.064 for HCl and 0.09 for NH_3 (Pringle et al., 2010a; Pringle
 255 et al., 2010b). v is the mean thermal velocity of the molecule and Δ is the mean free path length of
 256 the gas molecule (the distance from which the kinetic regime applies with respect to the
 257 particle). This information is then passed to the ISORROPIA-lite thermodynamic module to
 258 calculate the gas/aerosol partitioning. Specifically, the module receives as input the ambient
 259 temperature and humidity along with the diffusion-limited concentrations of H_2SO_4 , NH_3 , HNO_3 ,
 260 and HCl , the concentrations of the non-volatile cations (NVCs) Na^+ , K^+ , Ca^{2+} and Mg^{2+} , and the
 261 concentrations of the ions SO_4^{2-} , NO_3^- , NH_4^+ , and Cl^- present in the aerosol phase from the previous
 262 time step. The module then calculates the equilibrium reactions of the NO_3^- anion with the NVCs,
 263 depending on their abundance with respect to the SO_4^{2-} anion, taking into account mass
 264 conservation, electroneutrality, water activity equations and precalculated activity coefficients for
 265 specific ionic pairs (Fountoukis and Nenes, 2007; Kakavas et al., 2022). Therefore, in all cases
 266 where mineral dust is considered chemically active, all reactions of nitrate aerosols with NVC are
 267 treated. The salts that may be formed are assumed to be completely deliquesced as follows:



272
 273 Salt deliquescence over a range of relative humidities is treated by the Mutual Deliquescence
 274 Relative Humidity (MDRH) approach of Wexler and Seinfeld (1991). In a multicomponent salt
 275 mixture, the MDRH determines the humidity value above which all salts are considered to be
 276 saturated. In this study, if the wet aerosol is below the MDRH, it does not crystallize and remains
 277 in a supersaturated aqueous solution (Kakavas et al., 2022), with all salts completely deliquesced.
 278 More information on equilibrium reactions and equilibrium constants as well as the corresponding
 279 thermodynamic equilibrium calculations can be found in Fountoukis and Nenes (2007). It should
 280 be noted that in this study nitrate production on dust particles does not only occur via the
 281 thermodynamic equilibrium between gas-phase HNO_3 and particulate nitrate, but also via
 282 heterogeneous chemistry by hydrolysis of N_2O_5 on the dust surface. This chemical formation
 283 pathway is the most dominant for heterogeneous nitrate production (Seisel et al., 2005; Tang et
 284 al., 2012), while others, such as NO_2 oxidation during dust pollution events over polluted regions
 285 (Li et al., 2024), do not show such high yields under normal conditions. On the other hand,
 286 consideration of sulphate production by heterogeneous chemistry on dust would theoretically
 287 result in slightly reduced amounts of particulate nitrate in some cases due to acidification of dust

288 particles inhibiting partitioning of HNO_3 to the aerosol phase (Nenes et al., 2020). Overall, full
 289 consideration of heterogeneous chemistry on dust could change simulated nitrate aerosol
 290 concentrations only slightly and episodically, and therefore changes to radiative effect estimates
 291 are not expected to be critical.

292 The coating of dust particles by nitrate aerosols during gas/aerosol partitioning calculations is
 293 an important process that leads to an increase in dust solubility and hygroscopicity (Laskin et al.,
 294 2005). Therefore, after these processes have taken place, a large fraction of the originally insoluble
 295 dust particles has become soluble (Fig. 1a), which leads to changes in their optical properties, as
 296 their increased ability to absorb water makes them more efficient in extinguishing SW radiation
 297 and absorbing and emitting LW radiation (Fig. 1a, 1b) (Kok et al., 2023). The transfer to the soluble
 298 fraction after coating with soluble material is handled by the GMXe submodel, which also provides
 299 key aerosol attributes necessary for the calculation of the dust optical properties (see Section 2.3).
 300



301 **Figure 1:** Conceptual illustration of how dust-nitrate interactions affect the total NO_3^- (left) RE_{ari} and
 302 (right) RE_{aci} . **a.)** In dust-rich environments, nitric acid transported from anthropogenic pollution and biomass
 303 burning regions interacts with mineral cations to form a soluble coating on the surface of dust particles. The
 304 dominant effect of these interactions is an enhanced LW absorption (warming RE_{ari}) by the coarse dust
 305 particles. **b.)** In nitrate-rich environments, the intrusion of dust particles and their subsequent interaction
 306 with freshly formed nitric acid leads to an overall increase in aerosol hygroscopicity and thus a stronger
 307 SW reflection (cooling RE_{ari}). **c.)** In dust-rich environments, the number of ice crystals in cirrus clouds is
 308 reduced while their size is increased due to the interaction of dust particles with the transported HNO_3 . This
 309 results in an optical thinning of the ice clouds, which leads to less trapping of outgoing LW radiation
 310 (cooling RE_{aci}). **d.)** In nitrate-rich environments, the increased wet radius of aged dust particles leads to
 311 enhanced coagulation with smaller particles, resulting in a decrease in the number of smaller aerosols and,

312 in turn, a decrease in the number of activated particles in cloud droplets by smaller aerosols, which
313 ultimately leads to a reduction in the backscattering of SW radiation by warm clouds (warming RE_{ari}).
314

315
316 In general, the changes in the properties of dust particles through their interactions with nitrate
317 aerosols will result in more efficient removal rates, mainly through wet deposition, due to their
318 higher hygroscopicity and increased size (Fan et al., 2004). The reduced number of dust particles
319 that can act as ice nuclei (IN) and their increased size can lead to an optical thinning of cirrus
320 clouds (Fig. 1c) (Kok et al., 2023). Furthermore, the changes induced by dust-nitrate interactions
321 reduce the activation of smaller aerosols in warm clouds (Fig. 1d). In particular, the enhanced
322 hygroscopicity of dust particles will lead to a faster depletion of the available supersaturation, as
323 they act as giant CCN that absorb large amounts of water vapor to activate into cloud droplets
324 (Karydis et al., 2017). In addition, the population of smaller aerosols will also be depleted by
325 increased coagulation with the large dust particles. As a consequence of the different degrees of
326 complexity of the dust-nitrate interactions, it is very important to note that they do not always
327 result in a linear response in terms of how they affect climate through their subsequent interactions
328 with radiation, clouds, or both.
329

330 **2.3 Radiative Effect Calculation**

331 To calculate the global RE_{ari} and RE_{aci} of NO_3^- aerosols, the optical properties from the
332 AEROPT submodel and the radiative transfer calculations from the RAD submodel were used.
333 First, AEROPT provides the aerosol extinction (absorption and scattering) coefficients, the single
334 scattering albedo, and the aerosol asymmetry factor for each grid cell with a vertical distribution
335 analogous to the vertical resolution used. The GMXe submodel is used to provide input of aerosol
336 attributes for the calculation of aerosol optical properties, which is done online using 3D look-up
337 tables. The tables provide information on the real and imaginary parts of the refractive index and
338 the Mie size parameter per size mode (Dietmuller et al., 2016). Then, the radiative scheme of RAD
339 uses the particle number weighted average of the extinction cross section, the single scattering
340 albedo, and the asymmetry factor as input for the radiative transfer calculations. In addition to
341 AEROPT, RAD takes input from the submodels ORBIT (Earth orbital parameters), CLOUDOPT
342 (cloud optical properties) (Dietmuller et al., 2016), and IMPORT (import of external datasets) to
343 calculate the radiative transfer properties for longwave and shortwave radiation fluxes separately.
344 Both the AEROPT and RAD submodels can be invoked multiple times within a model time step,
345 each time with different settings for the aerosol optical properties, allowing radiative transfer
346 estimates for identical climatological conditions. This is of paramount importance for the
347 calculation of the RE_{ari} of aerosols since any effects due to possibly different climatological
348 conditions must be eliminated. Henceforth, all references to RE estimates, as well as net,
349 longwave, and shortwave flux quantities, will refer to the top of the atmosphere (TOA) only.

350 **2.3.1 Radiative Effect from Aerosol-Radiation Interactions (RE_{ari})**

351 To estimate the global RE_{ari} of all aerosols as well as that of total, coarse, and fine NO_3^- aerosols,
352 3 simulations were performed for each sensitivity case in Table 1. In the first simulation all aerosol
353 species are present. In the second simulation NO_3^- aerosols are completely removed by turning off
354 their formation by removing the pathway of HNO_3 formation through both NO_2 oxidation and

355 N₂O₅ hydrolysis, leaving no available HNO₃ to condense on the aerosol via equilibrium
 356 partitioning and form nitrate. In the third simulation, coarse mode NO₃⁻ aerosols are removed by
 357 allowing HNO₃ to condense only on the fine mode (i.e., the sum of the three smaller lognormal
 358 size modes: nucleation, Aitken, and accumulation). For each of these three simulations, the
 359 radiative transfer routines are called twice for each time step. One call uses the normal aerosol
 360 optical properties of the existing population, and the other call uses an aerosol optical depth equal
 361 to 0 to emulate an atmosphere without aerosols. Essentially, the global RE_{ari} of each simulation
 362 can be calculated by taking the difference between the net fluxes between the two calls. More
 363 specifically, the first simulation will yield the RE_{ari} of the total aerosol load ($F_{1,ari}$ hereafter), the
 364 second simulation will yield the RE_{ari} of all aerosols except NO₃⁻ ($F_{2,ari}$ below), and the third
 365 simulation will yield the RE_{ari} of all aerosols except the coarse mode NO₃⁻ ($F_{3,ari}$ below). Since the
 366 above estimates of the radiative effect were computed using the exact same climatology, its effect
 367 was effectively eliminated. However, in order to isolate the NO₃⁻ aerosol radiative effect, it is also
 368 essential to disable any aerosol-cloud interactions, otherwise the cooling effect would be severely
 369 underestimated because cloud scattering would make aerosol scattering less relevant (Ghan et al.,
 370 2012). For this purpose, the simplest cloud scheme available in the EMAC model is used, which
 371 calculates the cloud microphysics according to Lohmann and Roeckner (1996) who empirically
 372 relate the cloud droplet number concentration to the sulfate aerosol mass (Boucher and Lohmann
 373 1995) and specifically to its monthly mean values as derived from the sulfur cycle of the ECHAM5
 374 circulation model (Feichter et al., 1996). The cloud coverage is estimated according to Tompkins
 375 (2002) with the use of prognostic equations for the water phases and the distribution moments. To
 376 disable aerosol-cloud interactions, no aerosol activation routines are used to avoid coupling with
 377 the activation schemes. Overall, the global RE_{ari} of total, coarse, and fine NO₃⁻ aerosols are
 378 obtained as follows:

- 379 • $F_{NO3,ari}(F_{N,ari}) = F_{1,ari} - F_{2,ari}$
- 380 • $F_{coarseNO3,ari}(F_{cN,ari}) = F_{1,ari} - F_{3,ari}$
- 381 • $F_{fineNO3,ari}(F_{fN,ari}) = F_{3,ari} - F_{2,ari}$

382 **2.3.2 Radiative Effect from Aerosol-Cloud Interactions (RE_{aci})**

383 In this work we estimate the effect of total NO₃⁻ aerosols on the calculated global RE_{aci}.
 384 Climatology plays a crucial role in aerosol-cloud interactions and simulating a "fine-only NO₃⁻
 385 atmosphere", as done for the RE_{ari} calculations, would produce an unrealistic climatological
 386 scenario, since coarse-mode NO₃⁻ is strongly associated with cations in mineral dust particles
 387 (Karydis et al., 2016), making them quite effective as CCN (Karydis et al., 2017). Therefore, the
 388 RE_{aci} calculations require 2 additional simulations for each sensitivity case separately: one with all
 389 aerosols present and one with the entire NO₃⁻ aerosol load removed by turning off their formation
 390 as described in the previous section. The global RE_{aci} is then given by:

- 391 • $F_{NO3,aci}(F_{N,aci}) = FF_N - F_{N,ari}$

392 where FF_N is the total NO₃⁻ aerosol feedback radiative effect. Since $F_{N,ari}$ is calculated using the
 393 methodology described in Section 2.3.1, it is only necessary to estimate FF_N . This is equal to the
 394 difference in net fluxes between the two additional simulations. There is no need to emulate an
 395 aerosol-free atmosphere here since any differences induced by different climatologies must be

396 included. The two simulations performed for the calculation of FF_N use the cloud formation
397 scheme as described in Lohmann and Ferrachat (2010), which uses prognostic equations for the
398 water phases and the bulk cloud microphysics. In addition, the empirical cloud cover scheme of
399 Sundqvist et al. (1989) is used. For aerosol activation, the CDNC activation scheme of Morales
400 and Nenes (2014) is used, which includes the adsorption activation of mineral dust as described in
401 Karydis et al. (2017). The effect of dust-nitrate interactions on clouds presented here refers to the
402 lowest level of cloud formation at 940 hPa. For the ICNC activation, the scheme of Barahona and
403 Nenes (2009) is used, which calculates the ice crystal size distribution through heterogeneous and
404 homogeneous freezing as well as ice crystal growth.

405 **3. Radiative Effect from Aerosol-Radiation Interactions (RE_{ari})**

406 **3.1 Base Case**

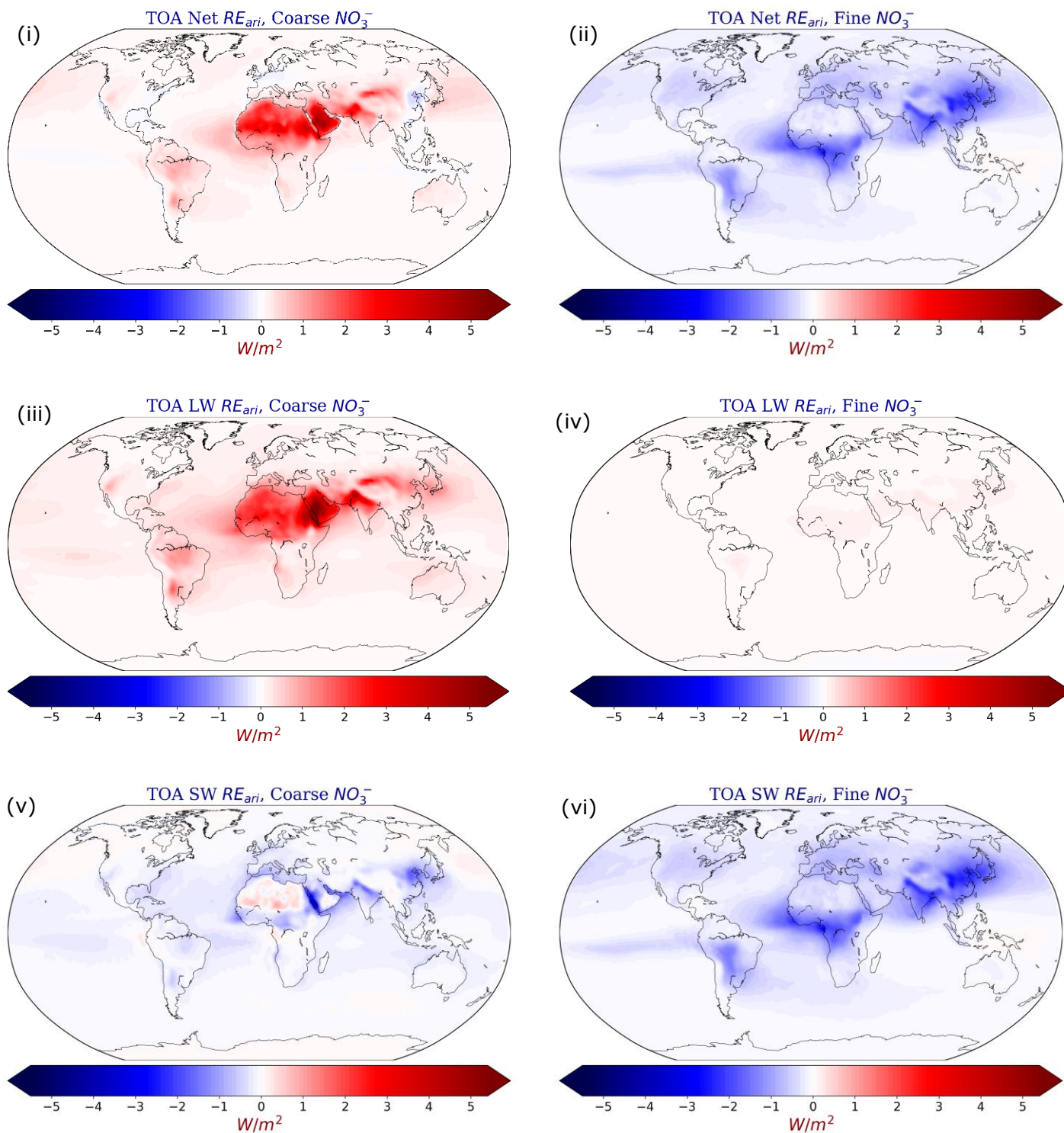
407 The global average RE_{ari} of total NO_3^- aerosols at the top of the atmosphere was found to be -
408 0.11 W/m^2 , which is within the reported range of the estimated present day all-sky direct radiative
409 effect of total NO_3^- aerosols by other studies (Liao et al., 2004; Bauer et al., 2007a; Bauer et al.,
410 2007b; Bellouin et al., 2011; Xu and Penner, 2012; Heald et al., 2014) (Table S4). The NO_3^-
411 cooling of the RE_{ari} calculated by EMAC is driven by the scattering of SW radiation (equal to -
412 0.34 W/m^2), which outweighs the warming due to absorption of LW radiation (equal to $+0.23$
413 W/m^2) (Table 2). The RE_{ari} of the total NO_3^- aerosol shows a clearly contrasting behavior with
414 respect to the size mode considered (Table 2; Figure 2).

415 In particular, the coarse particles show a net warming effect of $+0.17 \text{ W/m}^2$ (Fig. 2i) and
416 contribute to 96% of the LW warming of the total nitrate, while only contributing 15% of the
417 radiative cooling in the SW spectrum (-0.05 W/m^2). The LW warming is strongest over the dust
418 belt zone and especially over the Sahara, the Middle East and the northern face of the Himalayan
419 plateau, while the contribution over other arid regions such as the Atacama, Gobi, Taklimakan and
420 Mojave deserts is significant. These regions are characterized by moderate to high concentrations
421 of coarse NO_3^- aerosols due to the adsorption of HNO_3 on desert soil particles (Karydis et al., 2016;
422 Milousis et al., 2024). Therefore, the warming due to absorption of terrestrial LW radiation by
423 coarse-mode nitrates interacting with mineral dust is the strongest over these areas (see Fig. 1a),
424 ranging from $+1.5 \text{ W/m}^2$ to $+5 \text{ W/m}^2$ (Fig. 2iii). On the other hand, the cooling exerted by coarse
425 nitrate aerosol through the SW RE_{ari} is more pronounced over areas where it interacts strongly
426 with high concentrations of mineral dust particles (see Fig. 1b). Such areas include the Congo
427 Basin, where HNO_3 from tropical forest biomass burning interacts with Saharan mineral dust
428 particles; the Middle East and North Indian regions, where anthropogenic HNO_3 emissions interact
429 with mineral dust particles from the Sahara and Taklimakan deserts, respectively; and the East
430 Asian region, where HNO_3 emissions from Chinese megacities interact with mineral dust particles
431 from the Gobi Desert. These regions can lead to an average cooling of up to -3.5 W/m^2 (Fig. 2v).

432 Interestingly, there is no significant cooling from SW interactions over the Sahara for the coarse
433 mode. This phenomenon can be attributed to two factors, the first related to nitrate-dust
434 interactions and the second related to the characteristics of the region. Specifically, because the
435 underlying desert surface is very bright, its absorption in this part of the spectrum is less than that
436 of the particles above it, which means that the desert surface can scatter radiation more effectively
437 than the particles above it. This is further enhanced by the growth of coarse mode particles there

438 (see Fig. 4x and section 5.1) which increases the absorption cross section of the particles. All this
439 leads to an overall attenuation of the cooling effect over this region and sometimes even to local
440 warming (Fig. 2v).

441 In contrast to the radiative effect of coarse NO_3^- particles, the RE_{ari} of fine NO_3^- particles is an
442 overall cooling of -0.28 W/m^2 (Fig. 2ii). Fine nitrates have a negligible 4 % contribution to the
443 warming in the LW spectrum (Fig. 2iv) but account for 85 % of the net cooling of the total nitrate
444 aerosols (Fig. 2vi). The cooling induced by fine NO_3^- aerosols from scattering of SW radiation is
445 stronger (up to -5 W/m^2) over regions of high anthropogenic activity, particularly the East Asian
446 and Indian regions, where fine nitrates dominate the total nitrate aerosol load. The regions of West
447 Africa and the Amazon Basin are characterized by moderate fine nitrate concentrations, and the
448 cooling observed there is enhanced by HNO_3 associated with biomass burning interacting with
449 fresh and aged Saharan dust particles, respectively, which are dominated by accumulation mode
450 sizes in the absence of coarse mode nitrates. Finally, other polluted regions such as North America
451 and Europe also show SW cooling up to -2 W/m^2 .



452

453 **Figure 2:** Global mean TOA net RE_{ari} for (i) coarse and (ii) fine NO_3^- aerosols; longwave RE_{ari} for (iii)
 454 coarse and (iv) fine NO_3^- aerosols; shortwave RE_{ari} for (v) coarse and (vi) fine NO_3^- aerosols, as calculated
 455 by EMAC from the base case simulation.

456 **Table 2:** Net, longwave, and shortwave global mean TOA RE_{ari} of total, coarse, and fine NO₃⁻
 457 aerosols for the base case and each sensitivity case simulations.

458
 459

Simulation	Aerosol Component	TOA RE _{ari} (W/m ²)		
		Net	LW	SW
Base Case	Total NO ₃ ⁻	- 0.11	+ 0.23	- 0.34
	Coarse NO ₃ ⁻	+ 0.17	+ 0.22	- 0.05
	Fine NO ₃ ⁻	- 0.28	+0.01	- 0.29
Chemically Inert Dust	Total NO ₃ ⁻	- 0.09	+ 0.11	- 0.20
	Coarse NO ₃ ⁻	+ 0.07	+ 0.10	- 0.03
	Fine NO ₃ ⁻	- 0.16	+ 0.01	- 0.17
Homogeneous Ion Composition	Total NO ₃ ⁻	- 0.09	+ 0.18	- 0.27
	Coarse NO ₃ ⁻	+ 0.13	+ 0.17	- 0.04
	Fine NO ₃ ⁻	- 0.22	+ 0.01	- 0.23
Half Dust Scenario	Total NO ₃ ⁻	- 0.08	+ 0.19	- 0.27
	Coarse NO ₃ ⁻	+ 0.15	+ 0.18	- 0.03
	Fine NO ₃ ⁻	- 0.23	+ 0.01	- 0.24
Increased Dust Scenario	Total NO ₃ ⁻	- 0.10	+ 0.27	- 0.37
	Coarse NO ₃ ⁻	+ 0.20	+ 0.26	- 0.06
	Fine NO ₃ ⁻	- 0.30	+ 0.01	- 0.31

460

461 **3.2 Sensitivity of RE_{ari} Estimates**

462 The comparison of the calculated total NO₃⁻ radiative effect due to interactions with net, LW,
463 and SW radiation for the sensitivity cases listed in Table 1 can be found in Table 2, which shows
464 each of the estimates. Consideration of nitrate interactions with mineral dust cations can greatly
465 affect the NO₃⁻ RE_{ari} estimates. Assuming that mineral dust particles are inert, the estimated
466 warming due to LW radiation interactions for total nitrate aerosols is 52% weaker than in the base
467 case where dust reactivity is considered. Similarly, the cooling effect exerted by all nitrate aerosols
468 through interactions with SW radiation is estimated to be 41% weaker under the assumption that
469 mineral dust is non-reactive. Both estimates are lower when mineral dust is assumed to be
470 chemically inert, since HNO₃ is no longer effectively adsorbed on dust particles. However, since
471 both the estimated warming and cooling are weaker, the effects partially cancel each other out,
472 resulting in a net cooling effect (-0.09 W/m²) that is 18% weaker compared to the base case
473 calculations. Assuming a homogeneous ionic composition for the dust, results in SW cooling and
474 LW warming for total nitrate aerosols being 21% and 22% lower, respectively, weakening the
475 estimate for the net cooling RE_{ari} by 18% (-0.09 W/m²). The net direct radiative effect of total NO₃⁻
476 is the same for the cases where dust is assumed to have a homogeneous chemical composition and
477 where it has no chemical identity, indicating the importance of both aspects for the impact of dust-
478 nitrate interactions on the direct radiative effect.

479 In the Half Dust scenario, the total nitrate aerosol LW warming estimate is 17% weaker than in
480 the base case, while the total nitrate aerosol SW estimate is even more so (21%), resulting in a
481 lower net cooling estimate of -0.08 W/m². Finally, the Increased Dust scenario shows the strongest
482 total nitrate aerosol LW warming effect (17% increase over the base case) due to an increase in
483 coarse mode nitrate. At the same time, the cooling effect of total nitrate aerosols due to interactions
484 with SW radiation shows a smaller increase of 9%. Thus, accounting for the historical increase in
485 mineral dust emissions results in a net cooling estimate of -0.10 W/m², which is smaller than the
486 base case. Interestingly, the behavior of the global total NO₃⁻ RE_{ari} does not exhibit linearity with
487 respect to the global dust load. This is not surprising since the nitrate-dust interactions themselves
488 are not linearly correlated, and a given increase or decrease in dust emissions does not lead to an
489 analogous change in nitrate aerosol levels. For example, Karydis et al. (2016) have shown that
490 moving from a scenario in which nitrate-dust chemistry is not considered to one in which it is, but
491 with half dust emissions, resulted in a 39% increase in the tropospheric burden of nitrate aerosols.
492 However, moving from a scenario with half to full dust emissions, the corresponding increase was
493 only 9%. In our case, moving from the chemically inert dust scenario to the half dust scenario led
494 to an 18% increase in atmospheric nitrate aerosol burden, while moving from the half dust scenario
495 to the base case led to an additional 8% increase, and finally moving from the base case to the
496 increased dust scenario led to an even smaller increase of 5%.

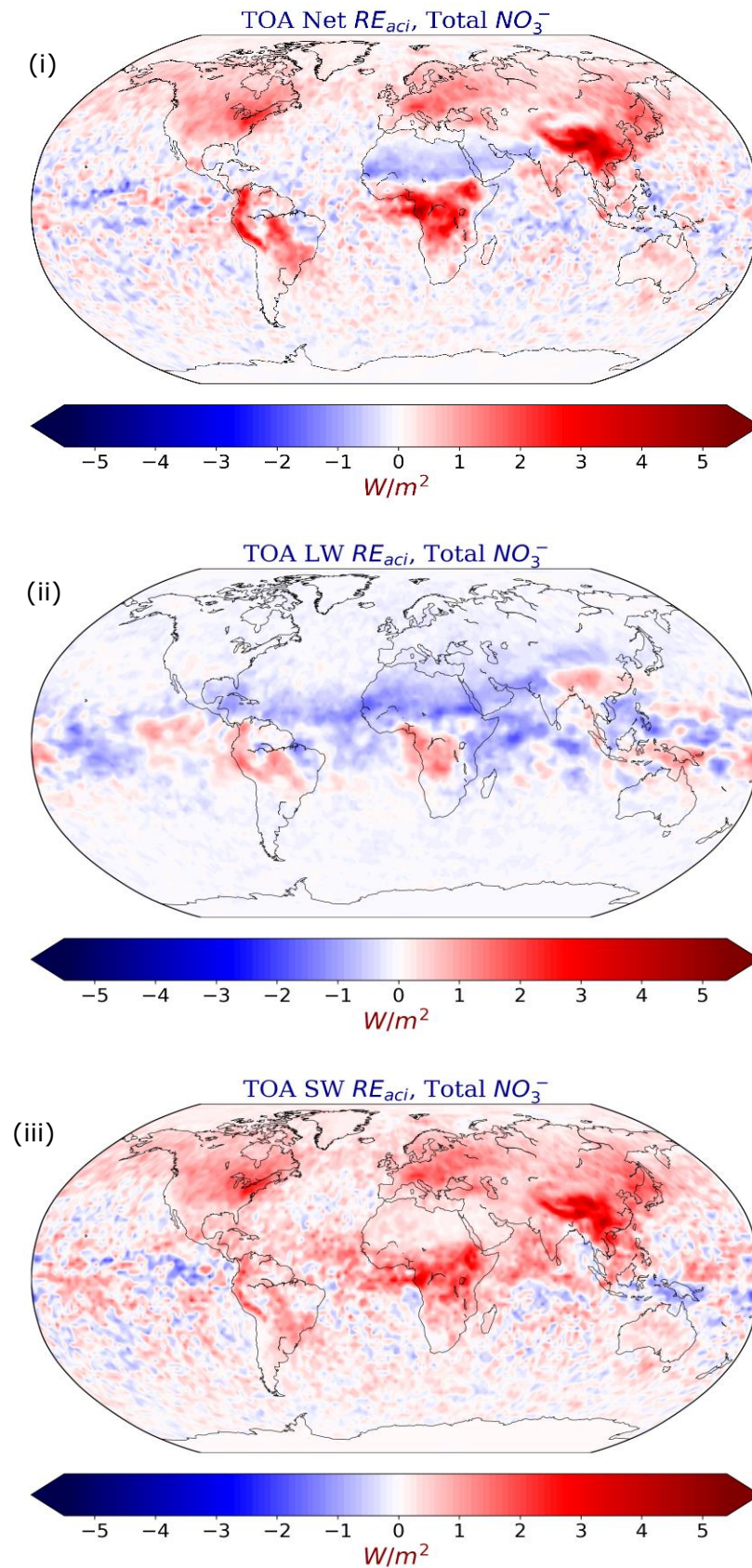
497 There are several reasons for this non-linearity between changes in dust load and nitrate
498 production. Firstly, since the adsorption of HNO₃ onto dust particles is the main driver of nitrate
499 production on dust, over desert areas (where the change in dust load takes place) the amount of
500 nitric acid present is the limiting factor for such production, rather than the amount of dust itself.
501 Secondly, when more dust is present in the atmosphere, the combination of its increased coating
502 with the higher aerosol numbers, tends to result in its more efficient removal by wet deposition as

503 well as coagulation. This inherently affects nitrate production, which does not increase in
504 proportion to the increase in dust.

505 **4 Radiative Effect from Aerosol-Cloud Interactions (RE_{aci})**

506 **4.1 Base Case**

507 The global average RE_{aci} of total NO_3^- aerosols at the top of the atmosphere was found to be
508 $+0.17 \text{ W/m}^2$. In contrast, an estimate of the RE_{aci} of nitrate aerosols by Xu and Penner (2012)
509 showed only a trivial cooling effect for particulate NO_3^- (-0.01 W/m^2). Similar to the RE_{ari} , the net
510 RE_{aci} estimated by EMAC is driven by the effect on the SW part of the spectrum, which causes a
511 warming effect of $+0.27 \text{ W/m}^2$, while the effect on the LW radiation causes an average cooling of
512 -0.10 W/m^2 (Table 3). Overall, the net RE_{aci} of total NO_3^- aerosols is reversed compared to the net
513 RE_{ari} , i.e. RE_{aci} exerts a strong cooling effect over regions where RE_{ari} exerts a warming effect and
514 vice versa (Fig. 3i). The reason for this is that the regions contributing to a cooling RE_{ari} are
515 dominated by smaller sized nitrate aerosols and vice versa. Therefore, the size characteristics of
516 the dominant nitrate aerosol population lead to different effects on the cloud optical properties as
517 discussed in section 1. For example, as the dominance of smaller nitrate aerosols decreases over a
518 particular region, the optical thinning of low-level clouds will have an opposite effect on the RE_{aci}
519 (Fig. 1d). Details of the mechanism by which nitrate-dust interactions affect cloud microphysical
520 processes are discussed in section 5. Over North America and Europe, RE_{aci} causes a warming
521 effect of up to $+3 \text{ W/m}^2$, driven solely by the effect on SW radiation (Fig. 3iii). Over the regions
522 of East Asia and the Amazon and Congo basins, RE_{aci} reaches a maximum of $+5 \text{ W/m}^2$, driven by
523 both the effect on the SW (up to $+4 \text{ W/m}^2$) and LW (up to $+1.5 \text{ W/m}^2$) parts of the radiation
524 spectrum. The cooling effect of RE_{aci} (up to -2 W/m^2) extends mainly between the equatorial line
525 and the Tropic of Cancer, mainly due to the interaction of nitrate aerosols with desert dust particles
526 (e.g. from the Sahara) and their effect on the terrestrial spectrum (LW) (Figs. 1c & 3ii). The cooling
527 effect of dust interactions with anthropogenic particles in the LW spectrum corroborates the
528 findings of Klingmüller et al. (2020) and is attributed to the reduced ice-water path due to the
529 depletion of small aerosols, which in turn leads to less trapped outgoing terrestrial radiation. In
530 addition, Kok et al. (2023) note how the presence of dust particles leads to an optical thinning of
531 cirrus clouds by reducing the number of ice crystals while increasing their size, which also leads
532 to less trapping of outgoing LW radiation and thus a cooling effect (Fig. 1c). On the other hand,
533 the warming effect of dust interactions with anthropogenic particles in the SW spectrum requires
534 further investigation and is therefore discussed in more detail in Section 5.



535 **Figure 3:** Global mean TOA RE_{aci} for total NO_3^- aerosols. Estimates for (i) net, (ii) longwave, and (iii)
 536 shortwave, as calculated by EMAC from the base case simulation.

537 **Table 3:** Net, longwave, and shortwave global mean TOA RE_{aci} of total NO_3^- aerosols for the
 538 base case and each sensitivity case simulations.

Simulation	TOA RE_{aci} (W/m^2)		
	Net	LW	SW
Base Case	+ 0.17	- 0.10	+ 0.27
Chemically Inert Dust	+ 0.11	- 0.06	+ 0.17
Homogeneous Ion Composition	+ 0.13	- 0.09	+ 0.22
Half Dust Scenario	+ 0.15	- 0.08	+ 0.23
Increased Dust Scenario	+ 0.14	- 0.11	+ 0.25

539

540 4.2 Sensitivity of RE_{aci} Estimates

541 Table 3 shows the comparison of the net, LW, and SW contributions of total NO_3^- to the RE_{aci}
 542 at the top of the atmosphere as calculated by the base case simulation and all sensitivity cases
 543 considered. By assuming a chemically inert dust, the calculated net RE_{aci} of nitrate decreases by
 544 35%, resulting in a net warming of $+0.11 W/m^2$. As with the RE_{ari} estimate, this sensitivity case
 545 produces the largest deviation from the base case among all sensitivity simulations, for both the
 546 SW (37% less warming) and LW (40% less cooling) estimates. This is due to the fact that the
 547 absence of dust-nitrate interactions does not have such a large impact on the population of both
 548 aerosols and activated particles (see also Section 5). The assumption of a homogeneous ionic
 549 composition of the mineral dust leads to a weakened LW cooling estimate of 10% and a weakened
 550 SW warming estimate of 19% resulting in a net NO_3^- RE_{aci} of $+0.13 W/m^2$ (24% lower than in the
 551 base case).

552 The reduced dust emissions result in a 15% weaker warming in the SW spectrum and a 20%
 553 weaker cooling in the LW spectrum, leading to an overall NO_3^- RE_{aci} of $+0.15 W/m^2$ (12% weaker
 554 than the base case scenario). This is because the reduced loading of nitrate aerosols, especially in
 555 the coarse mode, in the half dust scenario results in less absorption of LW radiation (Fig. 1c) (hence
 556 less cooling). Similarly, the effect of dust-nitrate interactions on the activation of smaller particles
 557 (Fig. 1d) is less drastic and results in a weaker inhibition of SW radiation scattering (hence less
 558 warming, see also Section 5). Finally, increased dust emissions in the increased dust scenario show
 559 a 10% increase in the LW cooling and an 8% decrease in the SW warming effect, surprisingly
 560 resulting in a net warming ($+0.14 W/m^2$) that is lower than in the half dust scenario. The reason
 561 that this scenario results in more LW cooling than the base case is that the increased amount of
 562 dust particles leads to even more optical thinning of the ice clouds, and therefore even less trapping
 563 of LW radiation (more cooling). However, the reason why the SW warming estimate is lower than
 564 the base case is more complicated. First, the transition from the half dust scenario to the base case
 565 and then to the increased dust scenario does not lead to an analogous increase in the nitrate aerosol

566 burden (see Section 3.2). Moreover, since the number of aerosols has increased from the increased
567 dust scenario to the base case, but the relative humidity has remained largely the same, there is
568 more competition for water vapor because it is now distributed over a larger population. As a
569 result, the wet radius increase in the presence of nitrates is not as strong in the increased dust
570 scenario compared to the base case, and the depletion of smaller sized particles is also not as strong
571 (not shown). The implications of the depletion of the aerosol population in the presence of nitrate
572 aerosols on the microphysical processes of warm clouds, and consequently on SW warming, are
573 discussed in the next section.

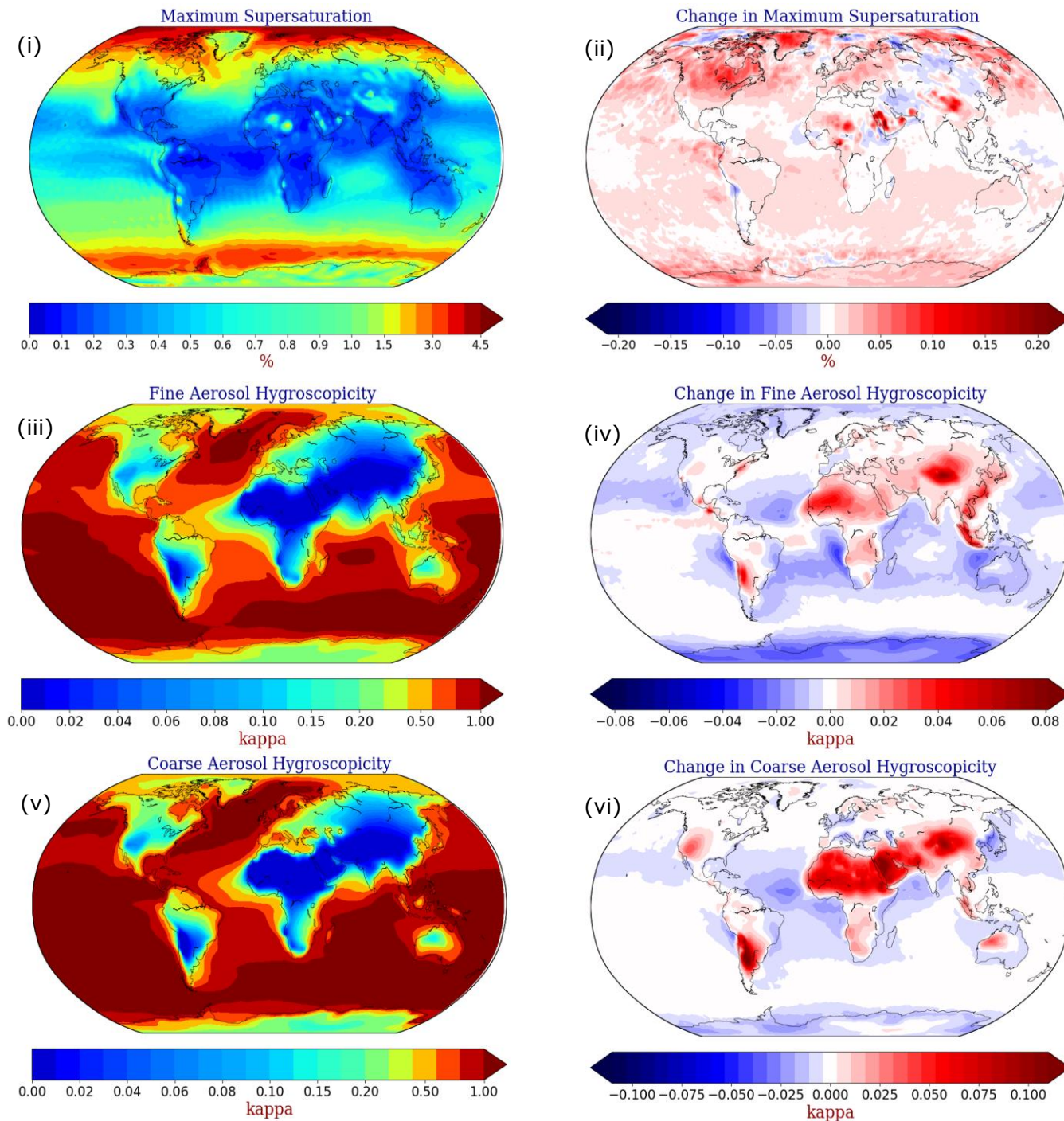
574 **5 Effect Of NO_3^- Aerosols on Cloud Microphysics**

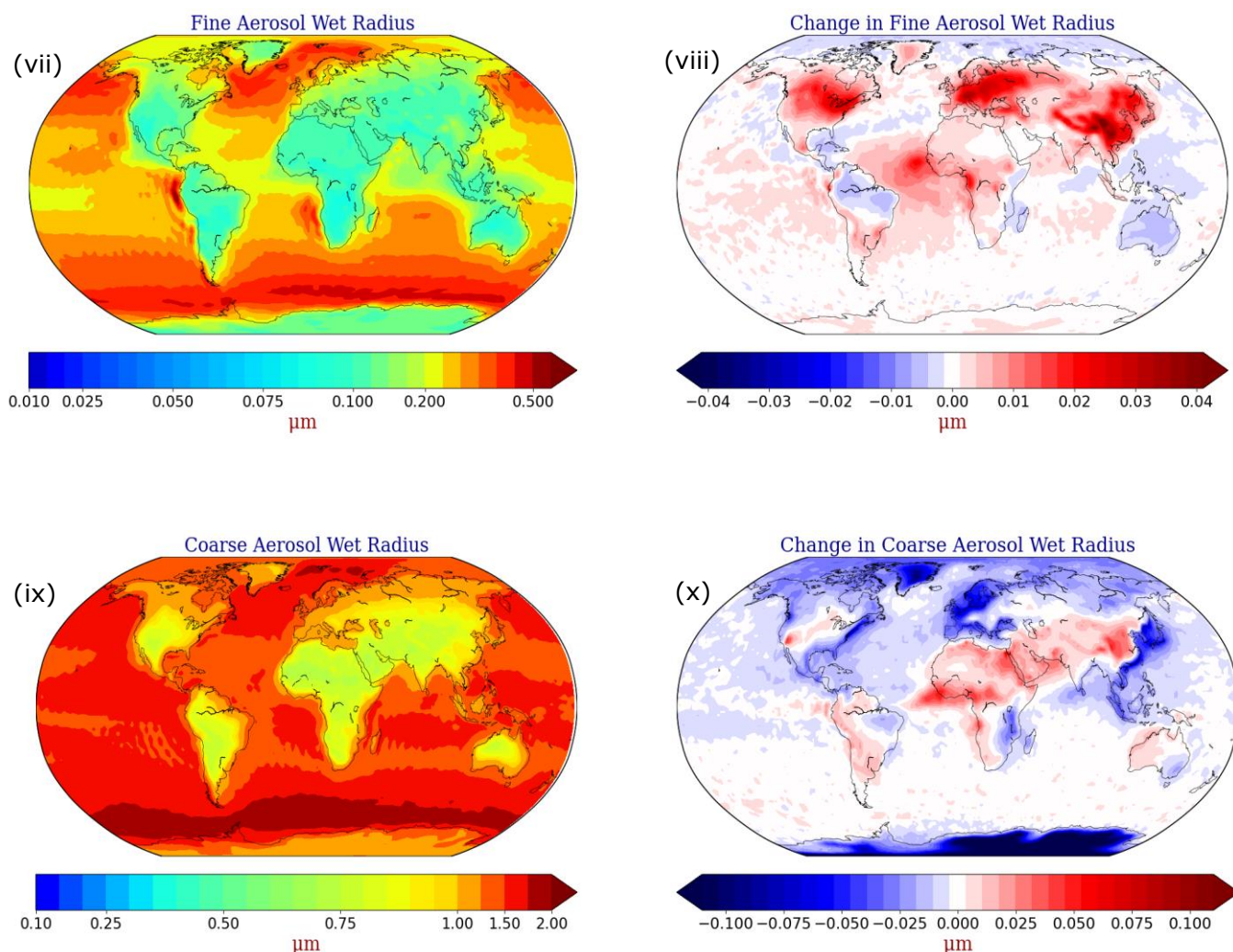
575 **5.1 Maximum Supersaturation, Hygroscopicity and Wet Radius**

576 To further investigate the cause of the positive RE_{aci} induced by the NO_3^- aerosols, their effect
577 on the aerosol population characteristics as well as on the cloud microphysics is investigated, with
578 respect to the lowest forming cloud level of 940 hPa. For this purpose, a sensitivity simulation is
579 performed assuming a 'nitrate aerosol free' (NAF) atmosphere, in which the formation of NO_3^-
580 aerosols has been switched off, but an advanced cloud scheme is considered which is the same as
581 the one described in Section 2.3.2. Essentially the same setup that was used for the estimation of
582 the total nitrate aerosol feedback radiative effect. This simulation is used to determine whether the
583 presence of NO_3^- aerosols has a significant effect on the hygroscopicity and size of atmospheric
584 aerosols and ultimately on the maximum supersaturation developed during cloud formation. Over
585 polluted areas affected by transported dust air masses from surrounding arid areas, the presence of
586 NO_3^- aerosols can increase the CCN activity of the large mineral dust particles, resulting in a
587 reduction of the maximum supersaturation and inhibiting the activation of the small anthropogenic
588 particles into cloud droplets (Klingmüller et al., 2020). Results from the NAF sensitivity
589 simulation support this hypothesis over parts of Eastern and Central Asia, where the maximum
590 supersaturation decreases by up to 0.05%. In contrast, the presence of NO_3^- aerosols increases
591 maximum supersaturation by up to 0.2% over North America, Europe, the Middle East, and parts
592 of southern Asia (Fig. 4ii). Therefore, changes in maximum supersaturation caused by the presence
593 of NO_3^- aerosols cannot explain their warming effect through the RE_{aci} .

594 The presence of NO_3^- has a significant effect on the hygroscopicity of both fine and coarse
595 aerosols and consequently on their wet radius, as shown in Figures 1a,b & 4. This is most evident
596 for coarse desert dust particles, which mix with NO_3^- aerosols from urban and forest regions,
597 increasing their hygroscopicity by an order of magnitude (up to 0.1), especially over the African-
598 Asian dust belt and the Atacama Desert in South America (Fig. 4vi). Aerosol hygroscopicity is
599 similarly increased for the fine mode particles both near arid regions and over the highly
600 industrialized region of Southeast Asia (Fig. 4iv). The low values of the hygroscopic parameter of
601 the fine aerosol population, especially over the dust belt zone, are largely due to the higher
602 proportion of insoluble fine particles present over these regions (Figure S5). This is also observed
603 over other regions with similarly low fine aerosol hygroscopicity (South Africa, South America
604 and Western U.S). Nevertheless, the estimates of aerosol kappa values at 940 hPa are broadly
605 consistent with the results of Pringle et al., (2010c). On the other hand, the aerosol hygroscopicity
606 for the two size modes is only slightly reduced, by up to 0.06 (or <10%) over the oceans and coasts
607 of Europe and East Asia, due to interactions of NO_3^- with sea salt particles, reducing their

608 hygroscopicity. The increased ability of both coarse dust aerosols and smaller aerosols to absorb
 609 water leads to an increase in their wet radius, but in different parts of the world. For example, fine
 610 particle sizes increase by up to $0.04 \mu\text{m}$ (up to 40%) mostly over regions of high anthropogenic
 611 activity (North America, Europe, and East Asia) (Fig. 4viii). On the other hand, coarse mode
 612 particle sizes are increased by up to $0.1 \mu\text{m}$ (up to 10%) over the forests of central Africa and the
 613 African-Asian dust belt zone (Fig. 4x), while showing a similar decrease near the coasts of the
 614 polluted northern hemisphere due to the effect of NO_3^- on the hygroscopicity of sea salt.





617 **Figure 4:** (i) Global mean maximum supersaturation, fine aerosol (iii) hygroscopicity and (v) wet
 618 radius, and coarse aerosol (vii) hygroscopicity and (ix) wet radius, as calculated by EMAC from
 619 the base case simulation at the altitude of 940 hPa. Absolute difference between base case and
 620 Nitrate Aerosol Free (NAF) sensitivity simulation in (ii) maximum supersaturation, fine aerosol
 621 (iv) hygroscopicity and (vi) wet radius, and coarse aerosol (viii) hygroscopicity and (x) wet radius
 622 at the altitude of 940 hPa. Red indicates higher values calculated by the base case simulation in
 623 the presence of NO_3^- aerosols.

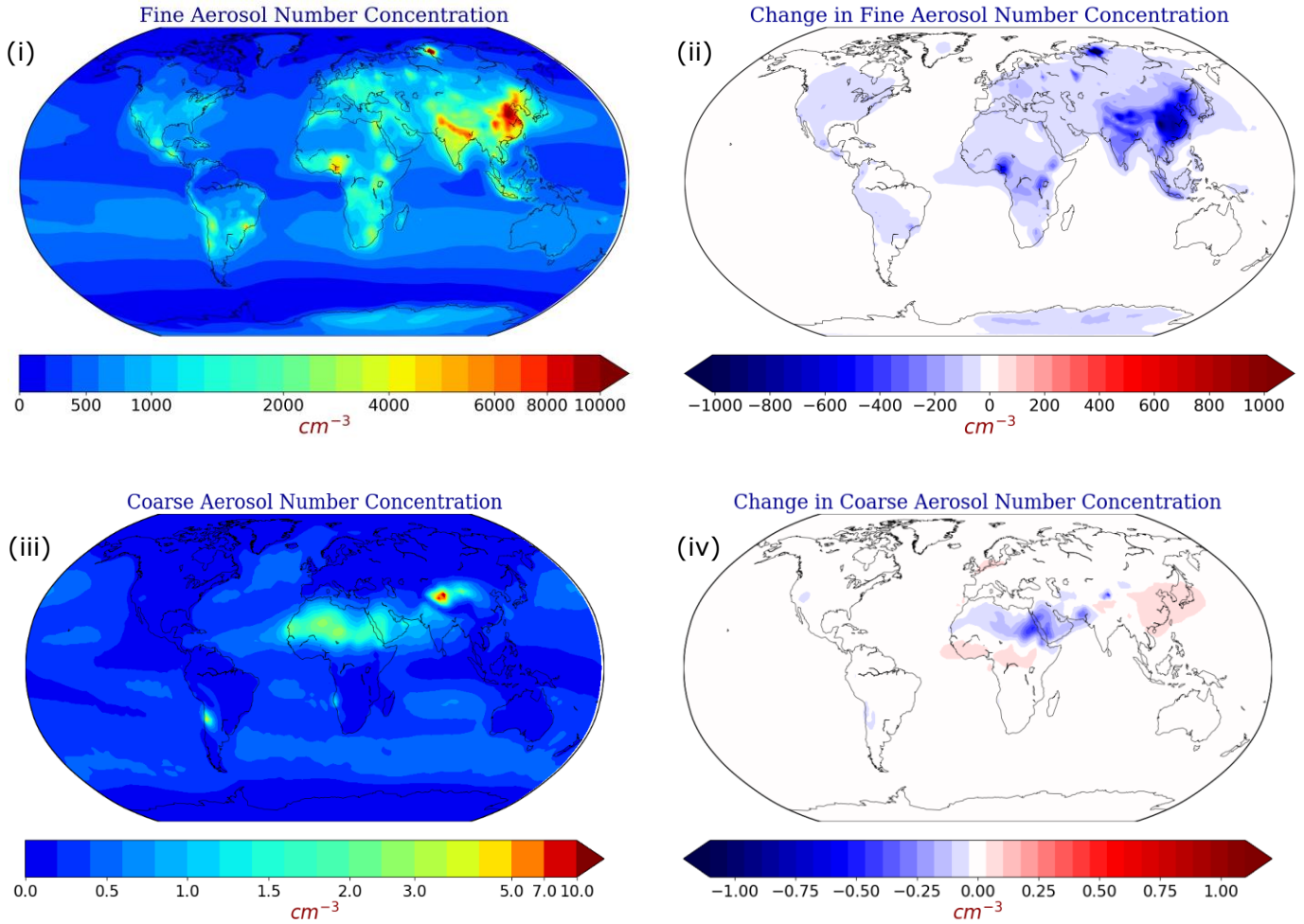
624 5.2 Number Concentrations of Aerosol and Activated Particles

625 Figure 5 shows the effect of NO_3^- on the number concentration of fine and coarse aerosols
 626 between the base case and the 'NAF' sensitivity simulation, as well as the total aerosol population.
 627 The presence of NO_3^- aerosols decreases the total aerosol number concentration over forests and
 628 polluted regions (see also Fig. 1d). This behavior is driven solely by the decrease in smaller particle
 629 sizes, as the effect is minimal for the coarser particles (Figs. 5ii & 5iv). The largest decrease is

630 calculated over East and South Asia (up to 1000 cm^{-3} or 10%), while decreases of up to 200 cm^{-3}
631 on average ($\sim 10\%$) are found over Europe, the USA, and Central Africa. This effect is directly
632 related to the increased wet radius of the aerosol population (Fig. 4viii) over these regions and thus
633 to its depositional efficiency. In addition, coarse dust particles become more hygroscopic due to
634 interactions with NO_3^- aerosols that increase in size, resulting in increased coagulation with the
635 smaller anthropogenic particles, which reduces their abundance.

636 The reduced aerosol number concentration in the presence of NO_3^- can lead to a reduction of
637 particles that are also activated into cloud droplets. Such behavior can be seen in Figure 6, which
638 shows the effect of NO_3^- on the number concentration of activated fine and coarse particles in
639 cloud droplets between the base case and the 'NAF' sensitivity simulation. The reduction in the
640 total number of activated cloud droplets is almost entirely due to the reduction in smaller size
641 particles (Figs. 6ii & 6iv). A reduction in the total number of activated droplets of up to 30 cm^{-3} or
642 10% is observed over the USA, Amazon, Europe, Central Africa, and parts of the Middle East,
643 while this reduction reaches up to 100 cm^{-3} (10%) over Southeast Asia, where the largest reductions
644 in aerosol numbers are also calculated (Fig. 4ii). In turn, these are the regions where the warming
645 effect of NO_3^- aerosols on the calculated mean RE_{aci} is strongest (Figure 3i). The small increase in
646 activated droplets ($\sim 10 \text{ cm}^{-3}$ or 1%) over Beijing, which concerns the fine mode particles, is most
647 likely because their number concentration decreases with increasing size. The high aerosol number
648 concentration there, which is the global maximum (Figure 5i), results in a hotspot of more readily
649 activated particles in the presence of NO_3^- . On the other hand, the CDNC decreases slightly over
650 the Sahara due to the more efficient deposition capacity of coarse dust particles due to their
651 interactions with nitrate aerosols, which is also reflected in the decrease in aerosol number (Fig.
652 6iv). Overall, the lower particle number in the presence of NO_3^- aerosols hinders the ability of the
653 smaller anthropogenic particles to activate into cloud droplets, leading to a reduced cloud cover
654 and thus a reduced cloud albedo effect. Therefore, not only less LW radiation is absorbed, but
655 more importantly, less SW radiation is scattered back to space, resulting in an overall warming of
656 the net average RE_{aci} for total NO_3^- aerosols.

657



658

659 **Figure 5:** Global mean number concentration of (i) fine and (iii) coarse aerosols as calculated by EMAC
 660 from the base case simulation at the altitude of 940 hPa. Absolute difference between the base case and the
 661 Nitrate Aerosol Free (NAF) sensitivity simulation in the number concentration of (ii) fine and (iv) coarse
 662 aerosols at the altitude of 940 hPa. Blue indicates that number concentrations are lower in the presence of
 663 NO_3^- aerosols.

664

665

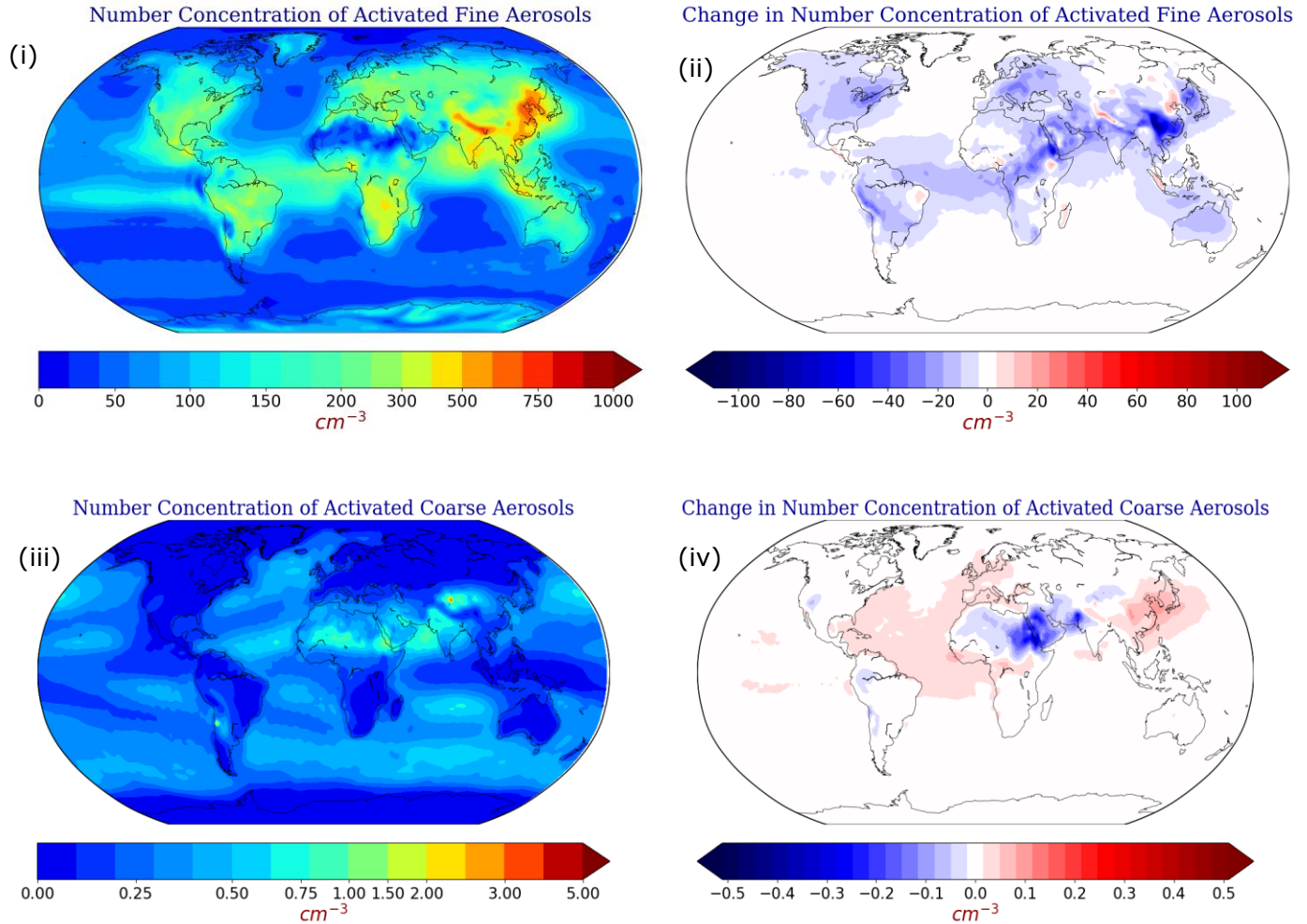
666

667

668

669

670



671

672 **Figure 6:** Global mean number concentration of activated (i) fine and (iii) coarse aerosols as calculated by
 673 EMAC from the base case simulation at the altitude of 940 hPa. Absolute difference between the base case
 674 and the Nitrate Aerosol Free (NAF) sensitivity simulation in the number concentration of activated (ii) fine
 675 and (iv) coarse aerosols at the altitude of 940 hPa. Blue indicates that number concentrations are lower in
 676 the presence of NO_3^- aerosols.

677

678 6. Conclusions and Discussion

679 This study presents the effects of interactions between mineral dust and NO_3^- aerosols on the
 680 present-day global TOA radiative effect of the latter. We investigate how the presence of dust
 681 affects the radiative effect of NO_3^- aerosols, both through aerosol interactions with radiation and
 682 separately with clouds (RE_{ari} and RE_{aci} , respectively). Sensitivity simulations are also performed,
 683 varying both the mineral dust composition and its emissions, to assess their effect on the calculated
 684 NO_3^- aerosol radiative effect.

685 It was found that the global average net RE_{ari} of total NO_3^- aerosols is $-0.11 W/m^2$, which is
 686 mainly due to the cooling from the shortwave part of the radiation spectrum due to scattering,

687 equal to -0.34 W/m^2 . A warming from the longwave part of the spectrum due to absorption was
688 found to be $+0.23 \text{ W/m}^2$ on global average and was mainly located over regions with high
689 concentrations of coarse NO_3^- aerosols. SW cooling was also observed in these regions, but also
690 over regions of high anthropogenic activity, mainly over the polluted northern hemisphere. The
691 behavior of the RE_{ari} was opposite when considering different sizes of NO_3^- aerosols. Specifically,
692 the coarse mode was responsible for 96% of the estimated warming in the LW part of the spectrum,
693 but 15% of the estimated cooling in the SW part of the spectrum. On the other hand, the
694 contribution of the fine mode to the LW warming was negligible, but it was the main contributor
695 to the SW cooling, accounting for 85% of the net estimate. The sensitivity experiments revealed
696 that the chemistry of the mineral dust is the most important factor in changing the estimated RE_{ari}
697 of the total NO_3^- aerosols. In particular, LW warming is most affected by this assumption, being
698 52% weaker after assuming chemically inert dust emissions, while the SW cooling is reduced by
699 41% compared to the base case simulation, amounting to a net cooling of -0.09 W/m^2 . A globally
700 homogeneous ionic composition for mineral dust had a smaller effect in LW (22% decrease) and
701 SW (21% decrease) but resulted in the same net estimate of -0.09 W/m^2 . Halving the dust
702 emissions resulted in weaker estimates for LW and SW by 17% and 21%, respectively, and the
703 lowest overall net RE_{ari} of -0.08 W/m^2 . On the other hand, a 50% increase in dust emissions
704 increased both LW warming and SW cooling by 17% and 9% respectively, resulting in a net
705 cooling RE_{ari} of -0.10 W/m^2 , indicating the strong non-linear relationship of nitrate-dust
706 interactions and how they affect the radiative effect estimates.

707 The global average net RE_{aci} of total NO_3^- aerosols was $+0.17 \text{ W/m}^2$ due to the effect on the
708 shortwave portion of the spectrum. This was found to be $+0.27 \text{ W/m}^2$, while the cooling from the
709 longwave part was -0.10 W/m^2 . Spatially, the net RE_{aci} is reversed compared to the net RE_{ari} for
710 total NO_3^- aerosols, where regions responsible for a strong SW cooling of the RE_{ari} contribute to a
711 strong SW warming of the RE_{aci} and vice versa. This is due to the fact that nitrate-dust interactions
712 challenge the dominance of smaller particles over heavily polluted regions, reducing the
713 reflectivity of warm cloud and thus having an opposite effect on the RE_{aci} . The sensitivity
714 experiments again showed that the consideration of the mineral dust chemistry is the most
715 important aspect for the calculation of the RE_{aci} of the total NO_3^- aerosols. When the dust was
716 assumed to be chemically inert, the LW and SW estimates were up to 40% weaker, resulting in a
717 net warming of $+0.11 \text{ W/m}^2$. Assuming a homogeneous ion composition resulted in a smaller
718 weakening of the estimates (up to 18%) and a net warming of $+0.13 \text{ W/m}^2$. When dust emissions
719 were halved, the LW cooling was reduced slightly more than in the base case, resulting in a net
720 warming of $+0.15 \text{ W/m}^2$. The 50% increase in dust emissions had the largest effect on LW behavior
721 (10% increase), but surprisingly the net estimate ($+0.14 \text{ W/m}^2$) was smaller than in the half-dust
722 scenario. The reason for this is that the SW estimate did not increase but decreased by 8% due to
723 the fact that in this scenario the increased nitrate burden causes increased competition for the
724 available supersaturation and the effect of dust-nitrate interactions on the smaller aerosol
725 populations is not as emphasized as in the base case.

726 The total NO_3^- aerosol RE_{aci} shows a positive sign, which is attributed to a reduced cloud albedo
727 effect. More specifically, although the presence or absence of NO_3^- aerosol in the atmosphere did
728 not significantly affect the total available maximum supersaturation, it did alter both the
729 hygroscopicity and wet radii of the aerosols. In the presence of NO_3^- , the hygroscopicity of aerosols

730 over deserts was increased by up to an order of magnitude, leading to an increase in their wet
731 radius of up to 10%, with an even larger increase of up to 40% for smaller particles over urban
732 regions. Therefore, in the presence of NO_3^- aerosols, the depletion of fine particles by coagulation
733 with coarser particles (i.e., mineral dust) is enhanced and further increases the size of the coarse
734 particles. The reduction in the number of aerosols is up to 10% in some regions, with maximum
735 reductions calculated over Southeast Asia. This reduction in the number of fine aerosols leads to
736 a reduction in the number of cloud droplets activated by fine aerosols (also up to 10%), which
737 would otherwise have absorbed more outgoing longwave radiation and, more importantly,
738 scattered more incoming shortwave radiation. Thus, the reduced cloud albedo effect leads to a
739 cooling in the longwave part of the spectrum, which is offset by a strong warming in the shortwave
740 part, overall resulting in a net warming of the atmosphere.

741 The chemistry-climate model simulations presented here suggest that NO_3^- aerosol-radiation
742 interactions lead to a net effect of -0.11 W/m^2 (cooling) driven by fine NO_3^- aerosol, while NO_3^-
743 aerosol-cloud interactions lead to a net effect of $+0.17 \text{ W/m}^2$ (warming) driven mainly by coarse
744 mode NO_3^- aerosol.

745

746 **Code and Data Availability**

747 The usage of MESSy (Modular Earth Submodel System) and access to the source code is licensed
748 to all affiliates of institutions which are members of the MESSy Consortium. Institutions can
749 become a member of the MESSy Consortium by signing the “MESSy Memorandum of
750 Understanding”. More information can be found on the MESSy Consortium website:
751 <http://www.messy-interface.org> (last access: 22 May 2024). The code used in this study has been
752 based on MESSy version 2.55 and is archived with a restricted access DOI
753 (<https://doi.org/10.5281/zenodo.8379120>, The MESSy Consortium, 2023). The data produced in
754 the study is available from the authors upon request.

755 **Acknowledgements**

756 This work was supported by the project FORCeS funded from the European Union’s Horizon 2020
757 research and innovation program under grant agreement No 821205. JFK was funded by the
758 National Science Foundation (NSF) Directorate for Geosciences grants 1856389 and 2151093.
759 The work described in this paper has received funding from the Initiative and Networking Fund of
760 the Helmholtz Association through the project “Advanced Earth System Modelling Capacity
761 (ESM)”. The authors gratefully acknowledge the Earth System Modelling Project (ESM) for
762 funding this work by providing computing time on the ESM partition of the supercomputer
763 JUWELS (Alvarez, 2021) at the Jülich Supercomputing Centre (JSC).

764 **Competing Interests**

765 At least one of the (co-)authors is a member of the editorial board of Atmospheric Chemistry and
766 Physics.

767 **Author Contributions**

768 AM and VAK wrote the paper with contributions from KK, APT, JFK, MK, and AN. VAK
769 planned the research with contributions from APT, MK and AN. AM, KK and VAK designed the
770 methodology for the radiative effect calculations. AM performed the simulations and analyzed the
771 results, assisted by VAK and APT. All the authors discussed the results and contributed to the
772 paper.

773

774 **REFERENCES**

- 775 Abdelkader, M., Metzger, S., Mamouri, R. E., Astitha, M., Barrie, L., Levin, Z., and Lelieveld, J.: Dust–air
776 pollution dynamics over the eastern Mediterranean, *Atmos. Chem. Phys.*, 15, 9173–9189,
777 <https://doi.org/10.5194/acp-15-9173-2015> , 2015.
- 778 Albrecht, B. A.: Aerosols, Cloud Microphysics, and Fractional Cloudiness, *Science*, 245(4923), 1227–1230,
779 <https://doi.org/10.1126/science.245.4923.1227> , 1989.
- 780 Alvarez, D.: JUWELS cluster and booster: Exascale pathfinder with modular supercomputing architecture
781 at juelich supercomputing Centre. *Journal of large-scale research facilities JLSRF*, 7, A183-A183,
782 <https://doi.org/10.17815/jlsrf-7-183>, 2021.
- 783 Arias, P.A., N. Bellouin, E. Coppola, R.G. Jones, G. Krinner, J. Marotzke, V. Naik, M.D. Palmer, G.-K.
784 Plattner, J. Rogelj, M. Rojas, J. Sillmann, T. Storelvmo, P.W. Thorne, B. Trewin, K. Achuta Rao, B.
785 Adhikary, R.P. Allan, K. Armour, G. Bala, R. Barimalala, S. Berger, J.G. Canadell, C. Cassou, A. Cherchi,
786 W. Collins, W.D. Collins, S.L. Connors, S. Corti, F. Cruz, F.J. Dentener, C. Derozynski, A. Di Luca, A.
787 Diongue Niang, F.J. Doblas-Reyes, A. Dosio, H. Douville, F. Engelbrecht, V. Eyring, E. Fischer, P.
788 Forster, B. Fox-Kemper, J.S. Fuglestedt, J.C. Fyfe, N.P. Gillett, L. Goldfarb, I. Gorodetskaya, J.M.
789 Gutierrez, R. Hamdi, E. Hawkins, H.T. Hewitt, P. Hope, A.S. Islam, C. Jones, D.S. Kaufman, R.E. Kopp, Y.
790 Kosaka, J. Kossin, S. Krakovska, J.-Y. Lee, J. Li, T. Mauritsen, T.K. Maycock, M. Meinshausen, S.-K. Min,
791 P.M.S. Monteiro, T. Ngo-Duc, F. Otto, I. Pinto, A. Pirani, K. Raghavan, R. Ranasinghe, A.C. Ruane, L.
792 Ruiz, J.-B. Sallée, B.H. Samset, S. Sathyendranath, S.I. Seneviratne, A.A. Sörensson, S. Szopa, I.
793 Takayabu, A.-M. Tréguier, B. van den Hurk, R. Vautard, K. von Schuckmann, S. Zaehle, X. Zhang, and
794 K. Zickfeld, 2021: Technical Summary. In *Climate Change 2021: The Physical Science Basis. Contribution of Working Group I to the Sixth Assessment Report of the Intergovernmental Panel on Climate Change* [Masson-Delmotte, V., P. Zhai, A. Pirani, S.L. Connors, C. Péan, S. Berger, N. Caud, Y. Chen, L. Goldfarb, M.I. Gomis, M. Huang, K. Leitzell, E. Lonnoy, J.B.R. Matthews, T.K. Maycock, T. Waterfield, O. Yelekçi, R. Yu, and B. Zhou (eds.)]. Cambridge University Press, Cambridge, United Kingdom and New York, NY, USA, <https://doi.org/10.1017/9781009157896.002> , 2021.
- 800 Astitha, M., Lelieveld, J., Kader, M. A., Pozzer, A., and de Meij, A.: Parameterization of dust emissions in
801 the global atmospheric chemistry-climate model EMAC: impact of nudging and soil properties,
802 *Atmospheric Chemistry and Physics* , 12(22), 11057–11083, [https://doi.org/10.5194/acp-12-11057-](https://doi.org/10.5194/acp-12-11057-2012)
803 [2012](https://doi.org/10.5194/acp-12-11057-2012) , 2012.
- 804 Bacer, S., Sullivan, S. C., Karydis, V. A., Barahona, D., Kramer, M., Nenes, A., Tost, H., Tsimpidi, A. P.,
805 Lelieveld, J., and Pozzer, A.: Implementation of a comprehensive ice crystal formation

parameterization for cirrus and mixed-phase clouds in the EMAC model (based on MESSy 2.53), Geoscientific Model Development , 11(10), <https://doi.org/10.5194/gmd-11-4021-2018> , 2018.

Barahona, D. and Nenes, A.: Parameterizing the competition between homogeneous and heterogeneous freezing in cirrus cloud formation - monodisperse ice nuclei, Atmospheric Chemistry and Physics , 9(16), 369-381, <https://doi.org/10.5194/acp-9-5933-2009> , 2009.

Barahona, D., West, R., Stier, P., Romakkaniemi, S., Kokkola, H., and Nenes, A.: Comprehensively accounting for the effect of giant CCN in cloud activation parameterizations, Atmospheric Chemistry and Physics , 10(5) , 2467-2473, <https://doi.org/10.5194/acp-10-2467-2010> , 2010.

Bauer, S. E., Koch, D., Unger, N., Metzger, S. M., Shindell, D. T., and Streets, D. G.: Nitrate aerosols today and in 2030: a global simulation including aerosols and tropospheric ozone, Atmospheric Chemistry and Physics , 7(19) , <https://doi.org/10.5194/acp-7-5043-2007> , 2007a.

Bauer, S. E., Mishchenko, M. I., Laci, A. A., Zhang, S., Perlwitz, J., and Metzger, S. M.: Do sulfate and nitrate coatings on mineral dust have important effects on radiative properties and climate modeling?, Journal of Geophysical Research: Atmospheres, 112(D6), <https://doi.org/10.1029/2005JD006977> , 2007b.

Bellouin, N., Rae, J., Jones, A., Johnson, C., Haywood, J., and Boucher, O.: Aerosol forcing in the Climate Model Intercomparison Project (CMIP5) simulations by HadGEM2-ES and the role of ammonium nitrate, Journal of Geophysical Research: Atmospheres, 116(D20) , <https://doi.org/10.1029/2011JD016074> , 2011.

Bond, T. C. and Bergstrom, R. W.: Light absorption by carbonaceous particles: An investigative review, Aerosol Science and Technology, 40(1), 27-67, <https://doi.org/10.1080/02786820500421521> , 2006.

Boucher, O., & Lohmann, U.: The sulfate-CCN-cloud albedo effect. *Tellus B: Chemical and Physical Meteorology*, 47(3), 281-300, <https://doi.org/10.3402/tellusb.v47i3.16048> , 1995.

Bouwman, A. F., Lee, D. S., Asman, W. A. H., Dentener, F. J., VanderHoek, K. W., and Olivier, J. G. J.: A global high-resolution emission inventory for ammonia, Global Biogeochemical Cycles , 11(4) , <https://doi.org/10.1029/97GB02266> , 1997.

Chang, D. Y., Lelieveld, J., Tost, H., Steil, B., Pozzer, A., & Yoon, J.: Aerosol physicochemical effects on CCN activation simulated with the chemistry-climate model EMAC, *Atmospheric Environment*, 162, 127-140, <https://doi.org/10.1016/j.atmosenv.2017.03.036> , 2017.

De Meij, A., Pozzer, A., Pringle, K. J., Tost, H., & Lelieveld, J.: EMAC model evaluation and analysis of atmospheric aerosol properties and distribution with a focus on the Mediterranean region, *Atmospheric research*, 114, 38-69, <https://doi.org/10.1016/j.atmosres.2012.05.014> , 2012.

Dentener, F., Kinne, S., Bond, T., Boucher, O., Cofala, J., Generoso, S., Ginoux, P., Gong, S., Hoelzemann, J. J., Ito, A., Marelli, L., Penner, J. E., Putaud, J. P., Textor, C., Schulz, M., van der Werf, G. R., and Wilson, J.: Emissions of primary aerosol and precursor gases in the years 2000 and 1750 prescribed data-sets for AeroCom, Atmospheric Chemistry and Physics , 6(12) , 4321-4344, <https://doi.org/10.5194/acp-6-4321-2006> , 2006.

Dietmuller, S., Jockel, P., Tost, H., Kunze, M., Gellhorn, C., Brinkop, S., Fromming, C., Ponater, M., Steil, B., Lauer, A., and Hendricks, J.: A new radiation infrastructure for the Modular Earth Submodel System (MESSy, based on version 2.51), Geoscientific Model Development, 9(6) , 2209-2222, <https://doi.org/10.5194/gmd-9-2209-2016> , 2016.

European Monitoring and Evaluation Programme (EMEP): EBAS database online, <https://projects.nilu.no/ccc/index.html> , last access: 3 September 2024.

Fan, S.-M., Horowitz, L. W., Levy II, H., and Moxim, W. J.: Impact of air pollution on wet deposition of mineral dust aerosols, Geophysical Research Letters, 31(2), <https://doi.org/10.1029/2003GL018501> , 2004.

Fanourgakis, G. S., Kanakidou, M., Nenes, A., Bauer, S. E., Bergman, T., Carslaw, K. S., Grini, A., Hamilton, D. S., Johnson, J. S., Karydis, V. A., Kirkevåg, A., Kodros, J. K., Lohmann, U., Luo, G., Makkonen, R.,

854 Matsui, H., Neubauer, D., Pierce, J. R., Schmale, J., Stier, P., Tsigaridis, K., van Noije, T., Wang, H.,
855 Watson-Parris, D., Westervelt, D. M., Yang, Y., Yoshioka, M., Daskalakis, N., Decesari, S., Gysel-Beer,
856 M., Kalivitis, N., Liu, X., Mahowald, N. M., Myriokefalitakis, S., Schrödner, R., Sfakianaki, M., Tsimpidi,
857 A. P., Wu, M., and Yu, F.: Evaluation of global simulations of aerosol particle and cloud condensation
858 nuclei number, with implications for cloud droplet formation, *Atmos. Chem. Phys.*, 19, 8591–8617,
859 <https://doi.org/10.5194/acp-19-8591-2019> , 2019.

860 Feichter, J., Kjellström, E., Rodhe, H., Dentener, F., Lelieveld, J., & Roelofs, G. J.: Simulation of the
861 tropospheric sulfur cycle in a global climate model. *Atmospheric Environment*, 30(10-11), 1693-1707,
862 [https://doi.org/10.1016/1352-2310\(95\)00394-0](https://doi.org/10.1016/1352-2310(95)00394-0), 1996.

863 Fountoukis, C. and Nenes, A.: ISORROPIA II: a computationally efficient thermodynamic equilibrium model
864 for $K^+Ca^{2+}Mg^{2+}NH_4^+Na^+SO_4^{2-}NO_3^-Cl^-H_2O$ aerosols, *Atmos. Chem. Phys.*, 7, 4639–4659,
865 <https://doi.org/10.5194/acp-7-4639-2007> , 2007.

866 Fuchs, N. A. and Davies, C. N.: The mechanics of aerosols, Pergamon Press, Oxford, ISBN
867 9780486660554, 1964.

868 Gao, M., Ji, D., Liang, F., and Liu, Y.: Attribution of aerosol direct radiative forcing in China and India to
869 emitting sectors, *Atmospheric Environment*, 190, 35-42,
870 <https://doi.org/10.1016/j.atmosenv.2018.07.011> , 2018.

871 Ghan, S. J., Liu, X., Easter, R. C., Zaveri, R., Rasch, P. J., Yoon, J. H., and Eaton, B.: Toward a Minimal
872 Representation of Aerosols in Climate Models: Comparative Decomposition of Aerosol Direct,
873 Semidirect, and Indirect Radiative Forcing, *Journal of Climate*, 25(19), 6461-6476,
874 <https://doi.org/10.1175/JCLI-D-11-00650.1>, 2012.

875 Grewe, V., Brunner, D., Dameris, M., Grenfell, J. L., Hein, R., Shindell, D., and Staehelin, J.: Origin and
876 variability of upper tropospheric nitrogen oxides and ozone at northern mid-latitudes, *Atmospheric
877 Environment*, 35(20), 3421-3433, [https://doi.org/10.1016/S1352-2310\(01\)00134-0](https://doi.org/10.1016/S1352-2310(01)00134-0) , 2001.

878 Hauglustaine, D. A., Balkanski, Y., and Schulz, M.: A global model simulation of present and future nitrate
879 aerosols and their direct radiative forcing of climate, *Atmospheric Chemistry and Physics*, 14(20),
880 11031-11063, <https://doi.org/10.5194/acp-14-11031-2014> , 2014.

881 Heald, C. L., Ridley, D. A., Kroll, J. H., Barrett, S. R. H., Cady-Pereira, K. E., Alvarado, M. J., and Holmes, C.
882 D.: Contrasting the direct radiative effect and direct radiative forcing of aerosols, *Atmos. Chem.
883 Phys.*, 14, 5513–5527, <https://doi.org/10.5194/acp-14-5513-2014> , 2014.

884 Hodzic, A., Bessagnet, B., & Vautard, R.: A model evaluation of coarse-mode nitrate heterogeneous
885 formation on dust particles. *Atmospheric Environment*, 40(22), 4158-4171,
886 <https://doi.org/10.1016/j.atmosenv.2006.02.015>, 2006.

887 Interagency Monitoring of Protected Visual Environment (IM-PROVE): Federal Land Manager
888 Environmental Database, <https://vista.cira.colostate.edu/Improve/improve-data/> ,last access: 3
889 September 2024.

890 IPCC, 2013: *Climate Change 2013: The Physical Science Basis*. Contribution of Working Group I to the
891 Fifth Assessment Report of the Intergovernmental Panel on Climate Change [Stocker, T.F., D. Qin, G.-
892 K. Plattner, M. Tignor, S.K. Allen, J. Boschung, A. Nauels, Y. Xia, V. Bex and P.M. Midgley (eds.)].
893 Cambridge University Press, Cambridge, United Kingdom and New York, NY, USA.

894 Jockel, P., Sander, R., Kerkweg, A., Tost, H., and Lelieveld, J.: Technical note: The Modular Earth
895 Submodel System (MESSy) - a new approach towards Earth System Modeling, *Atmospheric Chemistry
896 and Physics*, 5(2), 433-444, <https://doi.org/10.5194/acp-5-433-2005> , 2005.

897 Jockel, P., Tost, H., Pozzer, A., Bruhl, C., Buchholz, J., Ganzeveld, L., Hoor, P., Kerkweg, A., Lawrence, M.
898 G., Sander, R., Steil, B., Stiller, G., Tanarhte, M., Taraborrelli, D., Van Aardenne, J., and Lelieveld, J.:
899 The atmospheric chemistry general circulation model ECHAM5/MESSy1: consistent simulation of
900 ozone from the surface to the mesosphere, *Atmospheric Chemistry and Physics*, 6(12), 5067-5104,
901 <https://doi.org/10.5194/acp-6-5067-2006> , 2006.

902 Kakavas, S., Pandis, S. N., and Nenes, A.: ISORROPIA-Lite: A Comprehensive Atmospheric Aerosol
903 Thermodynamics Module for Earth System Models, *Tellus Series B-Chemical and Physical*
904 *Meteorology*, 74(1), 1-23, <https://doi.org/10.16993/tellusb.33> , 2022.

905 Kanakidou, M., Seinfeld, J. H., Pandis, S. N., Barnes, I., Dentener, F. J., Facchini, M. C., Van Dingenen, R.,
906 Ervens, B., Nenes, A., Nielsen, C. J., Swietlicki, E., Putaud, J. P., Balkanski, Y., Fuzzi, S., Horth, J.,
907 Moortgat, G. K., Winterhalter, R., Myhre, C. E. L., Tsigaridis, K., Vignati, E., Stephanou, E. G., and
908 Wilson, J.: Organic aerosol and global climate modelling: a review, *Atmospheric Chemistry and*
909 *Physics*, 5(4), 1053-1123, <https://doi.org/10.5194/acp-5-1053-2005> , 2005.

910 Karydis, V. A., Kumar, P., Barahona, D., Sokolik, I. N., and Nenes, A.: On the effect of dust particles on
911 global cloud condensation nuclei and cloud droplet number, *Journal of Geophysical Research:*
912 *Atmospheres*, 116, <https://doi.org/10.1029/2011JD016283>, 2011.

913 Karydis, V. A., Tsimpidi, A. P., Pozzer, A., Astitha, M., and Lelieveld, J.: Effects of mineral dust on global
914 atmospheric nitrate concentrations, *Atmospheric Chemistry and Physics*, 16(3), 1491-1509,
915 <https://doi.org/10.5194/acp-16-1491-2016> , 2016.

916 Karydis, V. A., Tsimpidi, A. P., Bacer, S., Pozzer, A., Nenes, A., and Lelieveld, J.: Global impact of mineral
917 dust on cloud droplet number concentration, *Atmospheric Chemistry and Physics*, 17(9), 5601-5621,
918 <https://doi.org/10.5194/acp-17-5601-2017> , 2017.

919 Kelly, J. T., Chuang, C. C., and Wexler, A. S.: Influence of dust composition on cloud droplet formation,
920 *Atmospheric Environment*, 41(14), 2904-2916, <https://doi.org/10.1016/j.atmosenv.2006.12.008> ,
921 2007.

922 Kerkweg, A., Buchholz, J., Ganzeveld, L., Pozzer, A., Tost, H., and Jockel, P.: Technical note: An
923 implementation of the dry removal processes DRY DEPosition and SEDimentation in the modular
924 earth submodel system (MESSy), *Atmospheric Chemistry and Physics*, 6(12), 4617-4632,
925 <https://doi.org/10.5194/acp-6-4617-2006> , 2006.

926 Khain, A. P. and Pinsky, M.: *Physical Processes in Clouds and Cloud Modeling*, Cambridge University
927 Press, ISBN 9781139049481, 2018.

928 Kirchstetter, T. W., Novakov, T., and Hobbs, P. V.: Evidence that the spectral dependence of light
929 absorption by aerosols is affected by organic carbon, *Journal of Geophysical Research: Atmospheres*,
930 109(D21), <https://doi.org/10.1029/2004JD004999> , 2004.

931 Klingmüller, K., Metzger, S., Abdelkader, M., Karydis, V. A., Stenchikov, G. L., Pozzer, A., and Lelieveld, J.:
932 Revised mineral dust emissions in the atmospheric chemistry-climate model EMAC (MESSy 2.52
933 DU_Astitha1 KKDU2017 patch), *Geoscientific Model Development*, 11(3), 989-1008,
934 <https://doi.org/10.5194/gmd-11-989-2018> , 2018.

935 Klingmüller, K., Lelieveld, J., Karydis, V. A., and Stenchikov, G. L.: Direct radiative effect of dust–pollution
936 interactions, *Atmospheric Chemistry and Physics*, 19(11), 7397-7408, [https://doi.org/10.5194/acp-](https://doi.org/10.5194/acp-19-7397-2019)
937 [19-7397-2019](https://doi.org/10.5194/acp-19-7397-2019) , 2019.

938 Klingmüller, K., Karydis, V. A., Bacer, S., Stenchikov, G. L., and Lelieveld, J.: Weaker cooling by aerosols
939 due to dust–pollution interactions, *Atmospheric Chemistry and Physics*, 20(23), 15285-15295,
940 <https://doi.org/10.5194/acp-20-15285-2020> , 2020.

941 Kok, J. F., Storelvmo, T., Karydis, V. A., Adebisi, A. A., Mahowald, N. M., Evan, A. T., He, C., and Leung, D.
942 M.: Mineral dust aerosol impacts on global climate and climate change, *Nature Reviews Earth &*
943 *Environment*, 4(2), 71-86, <https://doi.org/10.1038/s43017-022-00379-5> , 2023.

944 Krueger, B. J., Grassian, V. H., Cowin, J. P., & Laskin, A.: Heterogeneous chemistry of individual mineral
945 dust particles from different dust source regions: the importance of particle mineralogy. *Atmospheric*
946 *Environment*, 38(36), 6253-6261, <https://doi.org/10.1016/j.atmosenv.2004.07.010>, 2004.

947 Lance, S., Nenes, A., and Rissman, T. A.: Chemical and dynamical effects on cloud droplet number:
948 Implications for estimates of the aerosol indirect effect, *Journal of Geophysical Research:*
949 *Atmospheres*, 109(D22), <https://doi.org/10.1029/2004JD004596> , 2004.

950 Laskin, A., Wietsma, T. W., Krueger, B. J., and Grassian, V. H.: Heterogeneous chemistry of individual
951 mineral dust particles with nitric acid: A combined CCSEM/EDX, ESEM, and ICP-MS study, *Journal of*
952 *Geophysical Research: Atmospheres*, 110(D10), <https://doi.org/10.1029/2004JD005206> , 2005.

953 Li, J., Wang, W.-C., Liao, H., and Chang, W.: Past and future direct radiative forcing of nitrate aerosol in
954 East Asia, *Theoretical and Applied Climatology*, 121, 445-458, [https://doi.org/10.1007/s00704-014-](https://doi.org/10.1007/s00704-014-1249-1)
955 [1249-1](https://doi.org/10.1007/s00704-014-1249-1) , 2015.

956 Li, X., Yu, Z., Yue, M., Liu, Y., Huang, K., Chi, X., ... & Wang, M.: Impact of mineral dust photocatalytic
957 heterogeneous chemistry on the formation of the sulfate and nitrate: A modelling study over East
958 Asia. *Atmospheric Environment*, 316, 120166, <https://doi.org/10.1016/j.atmosenv.2023.120166>,
959 2024.

960 Liao, H., Seinfeld, J. H., Adams, P. J., and Mickley, L. J.: Global radiative forcing of coupled tropospheric
961 ozone and aerosols in a unified general circulation model, *Journal of Geophysical Research:*
962 *Atmospheres*, 109(D16), <https://doi.org/10.1029/2003JD004456> , 2004.

963 Lohmann, U. and Roeckner, E.: Design and performance of a new cloud microphysics scheme developed
964 for the ECHAM general circulation model, *Climate Dynamics*, 12, 557-572,
965 <https://doi.org/10.1007/BF00207939> , 1996.

966 Lohmann, U. and Feichter, J.: Global indirect aerosol effects: a review, *Atmospheric Chemistry and*
967 *Physics*, 5(3), <https://doi.org/10.5194/acp-5-715-2005> , 2005.

968 Lohmann, U. and Ferrachat, S.: Impact of parametric uncertainties on the present-day climate and on
969 the anthropogenic aerosol effect, *Atmospheric Chemistry and Physics*, 10(23),
970 <https://doi.org/10.5194/acp-10-11373-2010> , 2010.

971 Milousis, A., Tsimpidi, A. P., Tost, H., Pandis, S. N., Nenes, A., Kiendler-Scharr, A., and Karydis, V. A.:
972 Implementation of the ISORROPIA-lite aerosol thermodynamics model into the EMAC chemistry
973 climate model (based on MESSy v2.55): implications for aerosol composition and acidity,
974 *Geoscientific Model Development*, 17(3), 1111-1131, <https://doi.org/10.5194/gmd-17-1111-2024> ,
975 2024.

976 Morales Betancourt, R. and Nenes, A.: Understanding the contributions of aerosol properties and
977 parameterization discrepancies to droplet number variability in a global climate model, *Atmospheric*
978 *Chemistry and Physics*, 14(9), 4809-4826, <https://doi.org/10.5194/acp-14-4809-2014> , 2014.

979 Myhre, G., Samset, B. H., Schulz, M., Balkanski, Y., Bauer, S., Bernsten, T. K., Bian, H., Bellouin, N., Chin,
980 M., Diehl, T., Easter, R. C., Feichter, J., Ghan, S. J., Hauglustaine, D., Iversen, T., Kinne, S., Kirkevåg, A.,
981 Lamarque, J. F., Lin, G., Liu, X., Lund, M. T., Luo, G., Ma, X., van Noije, T., Penner, J. E., Rasch, P. J.,
982 Ruiz, A., Seland, Ø., Skeie, R. B., Stier, P., Takemura, T., Tsigaridis, K., Wang, P., Wang, Z., Xu, L., Yu, H.,
983 Yu, F., Yoon, J. H., Zhang, K., Zhang, H., and Zhou, C.: Radiative forcing of the direct aerosol effect
984 from AeroCom Phase II simulations, *Atmospheric Chemistry and Physics*, 13(4), 1853-1877,
985 <https://doi.org/10.5194/acp-13-1853-2013> , 2013.

986 Myhre, G., Shindell, D., and Pongratz, J.: Anthropogenic and natural radiative forcing, *Climate Change*
987 *2013-The Physical Science Basis*, 659-740, <https://dx.doi.org/10.1017/CBO9781107415324.018> ,
988 2014.

989 Nenes, A., Murray, B., Bougiatioti, A. (2014). Mineral Dust and its Microphysical Interactions with
990 Clouds. In: Knippertz, P., Stuut, JB. (eds) *Mineral Dust*. Springer, Dordrecht.
991 https://doi.org/10.1007/978-94-017-8978-3_12 , 2014.

992 Nenes, A., Pandis, S. N., Weber, R. J., and Russell, A.: Aerosol pH and liquid water content determine
993 when particulate matter is sensitive to ammonia and nitrate availability, *Atmos. Chem. Phys.*, 20,
994 3249–3258, <https://doi.org/10.5194/acp-20-3249-2020> , 2020.

995 Pozzer, A., Jockel, P. J., Sander, R., Williams, J., Ganzeveld, L., and Lelieveld, J.: Technical note: the
996 MESSy-submodel AIRSEA calculating the air-sea exchange of chemical species, *Atmospheric*
997 *Chemistry and Physics*, 6(12), 5435-5444, <https://doi.org/10.5194/acp-6-5435-2006> , 2006.

998 Pozzer, A., de Meij, A., Pringle, K. J., Tost, H., Doering, U. M., van Aardenne, J., and Lelieveld, J.:
999 Distributions and regional budgets of aerosols and their precursors simulated with the EMAC
1000 chemistry-climate model, *Atmos. Chem. Phys.*, 12, 961–987, [https://doi.org/10.5194/acp-12-961-](https://doi.org/10.5194/acp-12-961-2012)
1001 [2012](https://doi.org/10.5194/acp-12-961-2012), 2012.

1002 Pozzer, A., Reifenberg, S. F., Kumar, V., Franco, B., Kohl, M., Taraborrelli, D., Gromov, S., Ehrhart, S.,
1003 Jöckel, P., Sander, R., Fall, V., Rosanka, S., Karydis, V., Akritidis, D., Emmerichs, T., Crippa, M.,
1004 Guizzardi, D., Kaiser, J. W., Clarisse, L., Kiendler-Scharr, A., Tost, H., and Tsimpidi, A.: Simulation of
1005 organics in the atmosphere: evaluation of EMACv2.54 with the Mainz Organic Mechanism (MOM)
1006 coupled to the ORACLE (v1.0) submodel, *Geosci. Model Dev.*, 15, 2673–2710,
1007 <https://doi.org/10.5194/gmd-15-2673-2022>, 2022.

1008 Pringle, K. J., Tost, H., Message, S., Steil, B., Giannadaki, D., Nenes, A., Fountoukis, C., Stier, P., Vignati, E.,
1009 and Lelieveld, J.: Description and evaluation of GMXe: a new aerosol submodel for global simulations
1010 (v1), *Geoscientific Model Development*, 3(2), <https://doi.org/10.5194/gmd-3-391-2010>, 2010a.

1011 Pringle, K. J., Tost, H., Metzger, S., Steil, B., Giannadaki, D., Nenes, A., Fountoukis, C., Stier, P., Vignati, E.,
1012 and Lelieveld, J.: Corrigendum to "Description and evaluation of GMXe: a new aerosol submodel for
1013 global simulations (v1)" published in *Geosci. Model Dev.*, 3, 391–412, 2010, *Geoscientific Model*
1014 *Development*, 3(2), 413–413, <https://doi.org/10.5194/gmd-3-413-2010>, 2010b.

1015 Pringle, K. J., Tost, H., Pozzer, A., Pöschl, U., and Lelieveld, J.: Global distribution of the effective aerosol
1016 hygroscopicity parameter for CCN activation, *Atmos. Chem. Phys.*, 10, 5241–5255,
1017 <https://doi.org/10.5194/acp-10-5241-2010>, 2010c.

1018 Roeckner, E., Brokopf, R., Esch, M., Giorgetta, M., Hagemann, S., Kornblueh, L., Manzini, E., Schlese, U.,
1019 and Schulzweida, U.: Sensitivity of simulated climate to horizontal and vertical resolution in the
1020 ECHAM5 atmosphere model, *Journal of Climate*, 19(16), 3771–3791,
1021 <https://doi.org/10.1175/JCLI3824.1>, 2006.

1022 Sander, R., Baumgaertner, A., Cabrera-Perez, D., Frank, F., Gromov, S., Grooss, J. U., Harder, H., Huijnen,
1023 V., Jöckel, P., Karydis, V. A., Niemeyer, K. E., Pozzer, A., Hella, R. B., Schultz, M. G., Taraborrelli, D.,
1024 and Tauer, S.: The community atmospheric chemistry box model CAABA/MECCA-4.0, *Geoscientific*
1025 *Model Development*, 12(4), 1365–1385, <https://doi.org/10.5194/gmd-12-1365-2019>, 2019.

1026 Seinfeld, J. H. and Pandis, S. N.: *Atmospheric chemistry and physics from air pollution to climate change*,
1027 John Wiley & Sons, ISBN 1118947401, 2016.

1028 Seinfeld, J. H., Bretherton, C., Carslaw, K. S., Coe, H., DeMott, P. J., Dunlea, E. J., Feingold, G., Ghan, S.,
1029 Guenther, A. B., Kahn, R., Kraucunas, I., Kreidenweis, S. M., Molina, M. J., Nenes, A., Penner, J. E.,
1030 Prather, K. A., Ramanathan, V., Ramaswamy, V., Rasch, P. J., Ravishankara, A. R., Rosenfeld, D.,
1031 Stephens, G., and Wood, R.: Improving our fundamental understanding of the role of aerosol–cloud
1032 interactions in the climate system, *Proceedings of the National Academy of Sciences*, 113(21), 5781–
1033 5790, <https://doi.org/10.1073/pnas.1514043113>, 2016.

1034 Seisel, S., Börensén, C., Vogt, R., & Zellner, R.: Kinetics and mechanism of the uptake of N₂O₅ on
1035 mineral dust at 298 K. *Atmospheric Chemistry and Physics*, 5(12), 3423–3432,
1036 <https://doi.org/10.5194/acp-5-3423-2005>, 2005.

1037 Sposito, G.: *The Chemistry of Soils*, Oxford University Press, New York, ISBN 9780190630881, 1989.

1038 Sundqvist, H., Berge, E., and Kristjánsson, J. E.: Condensation and Cloud Parameterization Studies with a
1039 Mesoscale Numerical Weather Prediction Model, *Monthly Weather Review*, 117(8), 1641–1657,
1040 [https://doi.org/10.1175/1520-0493\(1989\)117%3C1641:CACPSW%3E2.0.CO;2](https://doi.org/10.1175/1520-0493(1989)117%3C1641:CACPSW%3E2.0.CO;2), 1989.

1041 Tang, M. J., Thieser, J., Schuster, G., & Crowley, J. N.: Kinetics and mechanism of the heterogeneous
1042 reaction of N₂O₅ with mineral dust particles. *Physical Chemistry Chemical Physics*, 14(24), 8551–
1043 8561, <https://doi.org/10.1039/C2CP40805H>, 2012.

1044 The Acid Deposition Monitoring Network in East Asia: EANET Data on the Acid Deposition in
1045 the East Asian Region, <https://monitoring.eanet.asia/document/public/index> , last access: 3
1046 September 2024.

1047 Tompkins, A. M.: A Prognostic Parameterization for the Subgrid-Scale Variability of Water Vapor and
1048 Clouds in Large-Scale Models and Its Use to Diagnose Cloud Cover, *Journal of the Atmospheric*
1049 *Sciences*, 59(12), 1917-1942, [https://doi.org/10.1175/1520-0469\(2002\)059%3C1917:APPFTS%3E2.0.CO;2](https://doi.org/10.1175/1520-0469(2002)059%3C1917:APPFTS%3E2.0.CO;2) , 2002.

1051 Tost, H., Jockel, P. J., Kerkweg, A., Sander, R., and Lelieveld, J.: Technical note: A new comprehensive
1052 SCAVenging submodel for global atmospheric chemistry modelling, *Atmospheric Chemistry and*
1053 *Physics*, 6(3), 565-574, <https://doi.org/10.5194/acp-6-565-2006> , 2006.

1054 Tost, H., Jöckel, P., and Lelieveld, J.: Lightning and convection parameterisations - uncertainties in global
1055 modelling, *Atmospheric Chemistry and Physics*, 7(17), 4553-4568, <https://doi.org/10.5194/acp-7-4553-2007> , 2007a.

1057 Tost, H., Jockel, P., Kerkweg, A., Pozzer, A., Sander, R., and Lelieveld, J.: Global cloud and precipitation
1058 chemistry and wet deposition: tropospheric model simulations with ECHAM5/MESSy1, *Atmospheric*
1059 *Chemistry and Physics*, 7(10), 2733-2757, <https://doi.org/10.5194/acp-7-2733-2007> , 2007b.

1060 Trump, E. R., Fountoukis, C., Donahue, N. M., and Pandis, S. N.: Improvement of simulation of fine
1061 inorganic PM levels through better descriptions of coarse particle chemistry, *Atmospheric*
1062 *Environment*, 102, 274-281, <https://doi.org/10.1016/j.atmosenv.2014.11.059> , 2015.

1063 Tsigaridis, K. and Kanakidou, M.: The present and future of secondary organic aerosol direct forcing on
1064 climate, *Current Climate Change Reports*, 4, 84-98, <https://doi.org/10.1007/s40641-018-0092-3> ,
1065 2018.

1066 Tsimpidi, A. P., Karydis, V. A., Pandis, S. N., and Lelieveld, J.: Global combustion sources of organic
1067 aerosols: model comparison with 84 AMS factor-analysis data sets, *Atmos. Chem. Phys.*, 16, 8939–
1068 8962, <https://doi.org/10.5194/acp-16-8939-2016> , 2016.

1069 Tsimpidi, A. P., Karydis, V. A., Pandis, S. N., and Lelieveld, J.: Global-scale combustion sources of organic
1070 aerosols: sensitivity to formation and removal mechanisms, *Atmos. Chem. Phys.*, 17, 7345–7364,
1071 <https://doi.org/10.5194/acp-17-7345-2017> , 2017.

1072 Twomey, S.: The Influence of Pollution on the Shortwave Albedo of Clouds, *Journal of Atmospheric*
1073 *Sciences*, 34, 1149-1152, [https://doi.org/10.1175/1520-0469\(1977\)034%3C1149:TIOPO%3E2.0.CO;2](https://doi.org/10.1175/1520-0469(1977)034%3C1149:TIOPO%3E2.0.CO;2)
1074 , 1977.

1075 Urdiales-Flores, D., Zittis, G., Hadjinicolaou, P., Osipov, S., Klingmüller, K., Mihalopoulos, N., Kanakidou,
1076 M., Economou, T., and Lelieveld, J.: Drivers of accelerated warming in Mediterranean climate-type
1077 regions, *npj Climate and Atmospheric Science*, 6(1), 97, <https://doi.org/10.1038/s41612-023-00423-1>
1078 , 2023.

1079 U.S. Environmental Protection Agency Clean Air Markets Division Clean Air Status and Trends Network
1080 (CASTNET): CASTNET Data, <https://www.epa.gov/castnet> , last access: 3 September 2024.

1081 Vignati, E., Wilson, J., and Stier, P.: M7: An efficient size-resolved aerosol microphysics module for large-
1082 scale aerosol transport models, *Journal of Geophysical Research: Atmospheres*, 109(D22),
1083 <https://doi.org/10.1029/2003JD004485> , 2004.

1084 Wexler, A. S., & Seinfeld, J. H.: Second-generation inorganic aerosol model. *Atmospheric Environment.*
1085 *Part A. General Topics*, 25(12), 2731-2748, [https://doi.org/10.1016/0960-1686\(91\)90203-J](https://doi.org/10.1016/0960-1686(91)90203-J), 1991.

1086 Wong, J. P. S., Tsagkaraki, M., Tsiodra, I., Mihalopoulos, N., Violaki, K., Kanakidou, M., Sciare, J., Nenes,
1087 A., and Weber, R. J.: Atmospheric evolution of molecular-weight-separated brown carbon from
1088 biomass burning, *Atmospheric Chemistry and Physics*, 19(11), 7319-7334,
1089 <https://doi.org/10.5194/acp-19-7319-2019> , 2019.

1090 Xu, L. and Penner, J. E.: Global simulations of nitrate and ammonium aerosols and their radiative effects,
1091 *Atmospheric Chemistry and Physics*, 12(20), <https://doi.org/10.5194/acp-12-9479-2012> , 2012.

1092 Yienger, J. J. and Levy, H.: EMPIRICAL-MODEL OF GLOBAL SOIL-BIOGENIC NOX EMISSIONS, Journal of
1093 Geophysical Research: Atmospheres, 100(D6), <https://doi.org/10.1029/95JD00370> , 1995.
1094 Zhang, Y., Forrister, H., Liu, J., Dibb, J., Anderson, B., Schwarz, J. P., Perring, A. E., Jimenez, J. L.,
1095 Campuzano-Jost, P., Wang, Y., Nenes, A., and Weber, R. J.: Top-of-atmosphere radiative forcing
1096 affected by brown carbon in the upper troposphere, Nature Geoscience, 10(7),
1097 <https://doi.org/10.1038/ngeo2960> , 2017.
1098 Zhang, B.: The effect of aerosols to climate change and society, Journal of Geoscience and Environment
1099 Protection, 8(08), 55, <https://doi.org/10.4236/gep.2020.88006> , 2020.
1100
1101